



Doctoral Thesis in Materials Science and Engineering

Creep Behavior of High Temperature Cast Materials for Exhaust Applications

CHRISTIAN ÖBERG

Creep Behavior of High Temperature Cast Materials for Exhaust Applications

CHRISTIAN ÖBERG

Academic Dissertation which, with due permission of the KTH Royal Institute of Technology, is submitted for public defence for the Degree of Doctor of Philosophy on Friday the 18th of december 2020, 09.00, Public defense by Zoom.

Doctoral Thesis in Materials Science and Engineering
KTH Royal Institute of Technology
Stockholm, Sweden 2020

© Christian Öberg

© Christian Öberg, Baohua Zhu, Stefan Jonsson, Paper 1.

© Christian Öberg, Ralf Rablbauer, Baohua Zhu, Stefan Jonsson, Paper 2.

© Christian Öberg, Baohua Zhu, Stefan Jonsson, Paper 3.

© Christian Öberg, Baohua Zhu, Stefan Jonsson, Paper 4.

© Christian Öberg, Baohua Zhu, Stefan Jonsson, Paper 5.

ISBN 978-91-7873-728-4

TRITA-ITM-AVL 2020:48

Printed by: Universitetsservice US-AB, Sweden 2020

Author's contribution to appended papers

Appendix 1: "Plastic deformation and Creep of Two Ductile Cast irons, Simo51 and Simo1000, during Thermal Cycling with Large Strains".

Literature survey, mechanical testing, microscopy, wrote the paper with modifications from supervisors.

Appendix 2: "Monotonic and Cyclic Creep of Cast Materials for Exhaust Manifolds"

Literature survey, mechanical testing associated with SRTC (stress relaxations with thermal cycling), planning of STT (sequential tensile testing) and CL (constant load) creep tests, data analyses associated with all test methods, SEM-microscopy, wrote the paper with modifications from supervisors.

Appendix 3: "Creep, strain and oxidation damage in the ferritic ductile cast iron SiMo51 at 700°C"

Literature survey, tensile testing, oxidation testing, planning of CL tests, did data analyses associated with all tests, microscopic imaging associated with LOM and regular SEM, did EBSD microscopy together with Joacim Hagström, post-processing of EBSD-data, took part in the discussion of the results of the thermodynamic calculations, wrote the paper, except thermodynamic part, with modifications from supervisors.

Appendix 4: "Creep behaviour, creep damage and precipitation in the austenitic cast steel HK30 at 750°C"

Literature survey, planning of the CL tests, data analyses, microscopic analyses associated with LOM and regular SEM, did EBSD microscopy together with Joacim Hagström, post-processing of EBSD-data, took part in the discussions of the results of the thermodynamic Scheil simulation, wrote the paper, except Scheil simulation part, with modifications from supervisors.

Appendix 5: "Creep behaviour, creep damage and precipitation in the austenitic ductile cast iron D5S at 750°C"

Literature survey, planning of the CL tests, data analyses, LOM-imaging, EBSD microscopy together with Joacim Hagström, post-processing of EBSD-data, wrote the paper with modifications from supervisors.

Sammanfattning

Avhandlingen fokuserar på krypbeteende hos fyra gjutna material som används till avgasgrenrör i lastbilmotorer. Dessa material inbegriper två ferritiska segjärn, betecknade SiMo51 och SiMo1000, ett austenitiskt segjärn, D5S, och ett austenitiskt gjutstål, HK30. Gjutjärnen är rika på kol och har en mikrostruktur som utöver matrisen består av grafitnoder och olika utskiljningar, de senare huvudsakligen karbider och intermetalliska faser. Gjutstålet har ett lägre kolinnehåll och saknar därför grafitnoder, men innehåller andra utskiljningar. Under drift cyklas avgasgrenrören termiskt upp till 800 °C i ett låst tillstånd, eller mer specifikt fastskruvade till motorblocket. Lastfallet och miljön ger upphov till krypdeformation, utmattning, oxidation och andra förändringar i mikrostrukturen. Generellt sett har utvecklingen mot mer miljövänliga lastbilmotorer lett till högre avgastemperaturer vilket i sin tur innebär högre krav på materialen.

Det huvudsakliga målet med studien var att utreda krypbeteende och relaterade fenomen hos de inkluderade materialen (se ovan). Ett sekundärt mål var även att jämföra resultat från tre olika typer av kryptester: i) SRTC (stress relaxations with thermal cycling) är ett sätt att framkalla spänningsrelaxationer i materialet genom att cykla det termiskt i ett låst tillstånd, ii) STT (sequential tensile test) är ett dragprov vid konstant temperatur under vilket töjningshastigheten ändras vid givna töjningsnivåer, iii) CL (constant-load creep test) är den traditionella krypprovningsmetoden, som innebär konstant last och temperatur. SRTC och STT är avsedda som snabba och billiga krypprovningsmetoder medan CL-metoden generellt betraktas som långsam och dyr. Resultat från de tre metoderna jämfördes regelmässigt i s.k Norton plots, det vill säga logaritmiska krypdiagram med spänning och töjningshastighet.

Resultat från i) SRTC (i kompression) och ii) STT (i drag) överensstämde generellt mycket väl vilket indikerar att krypning i materialen inte beror av lastriktning. Utöver detta var töjningshastigheten som registrerades i SRTC-testerna konstant med antalet cykler. Båda dessa upptäckter underlättar modellering av cyklisk krypning i materialen, ett ämne som dock inte ingick i avhandlingen. Det finns diskrepanser mellan den krypdata som erhöles med CL-metoden och den som erhöles med de snabbare metoderna (STT och SRTC). Dessa kunde inte fullt ut förklaras, men olika alternativ diskuterades. Hursomhelst är det givet att den tidsberoende krypskada som utvecklas under ett långsamt krypprov (CL) inte kan uppstå efter snabba spänningsrelaxationer eller dragprov.

De mikrostrukturella förändringar som skedde under krypning dokumenterades genom LOM-, SEM- och EBSD-mikroskopi, med flera olika tekniker för preparering och etsning.

I CL-provning vid 700 °C uppvisade SiMo51 primärkryp som mer eller mindre direkt följdes av tertiärkryp. Tertiärkryptet var i sin tur uppdelat i två subregimer, av vilka den första associerades med skada från kaviteter runt grafitnoder och runt korngränser/karbider, och den andra med större sprickor mellan grafitnodulerna. Den oxidation som skedde under krypning var påtaglig, men inte tillräcklig för att förklara uppdelningen i två tertiärkrypregimer. Oxidationen på provytan och runt nodulerna studerades explicit. Oxiden som helhet bestod av flera individuella lager som kunde identifieras genom att kombinera EDX-data och termodynamiska beräkningar.

Både D5S och HK30 CL-testades vid 750 °C för att reflektera en högre driftstemperatur hos dessa material jämfört med SiMo51. Efter långvarig krypexponering uppvisade HK30 typiska krypkaviteter vid korngränserna, utskiljning av sigma-fas och G-fas, små oxidinträningar och ett tunt rekristalliserat lager på provytan. D5S å sin sida uppvisade olika typer av kaviteter/porer runt grafitnodulerna, liknande den skada som noterades för SiMo51 vid 700 °C. Brottmekanismen bestod av skjuvsprickor som propagerade mellan grafitnodulerna. Olika utskiljningar bildades under krypexponeringen.

Abstract

This thesis focuses on creep of four cast materials intended for exhaust manifolds in heavy-duty truck engines. Two of the materials are ferritic ductile cast irons, SiMo51 and SiMo1000, one is an austenitic ductile cast iron, D5S, and another one is an austenitic cast steel, HK30. The ductile cast irons, rich in carbon, have a microstructure with graphite nodules and precipitates, mainly carbides and intermetallics. The cast steel, on the other hand, being meagre in carbon, has precipitates but lacks graphite nodules. During service, the exhaust components are thermally cycled up to 800 °C in a locked stated, bolted to an engine block. This gives rise to creep deformation, fatigue, oxidation and microstructural changes. Driven by the development of environmental friendly engines of lower emissions, the exhaust gas temperature is increasing, continuously leading to higher demands on the materials.

The main aim was to investigate the creep behavior and related phenomena of the included materials. A secondary aim was to compare results from three types of tests, i) SRTC (stress relaxations with thermal cycling), provoking stress relaxations in a locked specimen subjected to thermal cycling, ii) STT (sequential tensile test), changing the strain rate at selected strain levels during a tensile test at a selected temperature, iii) CL (constant-load creep test), i.e. traditional creep testing, applying a constant load at a given temperature. SRTC and STT are intended as quick and cheap methods while CL is generally considered slow and associated with high costs. Results of the three methods were regularly compared in Norton plots, i.e. double logarithmic plots of stress and strain rate.

Results of i) SRTC (in compression) and ii) STT (in tension) were generally in very close agreement which indicates that creep of the included materials is independent of loading direction. In addition, the creep rates obtained by SRTC were also constant with number of cycles. Both findings facilitate modeling of cyclic creep, although this was not in the scope of the present thesis. There were discrepancies between data sets of CL and SRTC/STT which could not be explained, although several reasons were discussed. In addition, the time-dependent creep damage which develops during a slow CL test is always missed in quick stress relaxation tests or tensile tests.

The microstructural events taking place during creep were documented using LOM, SEM and EBSD microscopy techniques, with various etching and sample preparation procedures.

When CL tested at 700 °C, SiMo51 showed primary creep, more or less directly followed by tertiary creep. The tertiary creep regime was in turn divided into two stages of which the first was associated with the formation of typical creep cavities around the graphite nodules and at the grain boundaries, and the second associated with larger cracks between the graphite nodules. Oxidation was significant but not enough to be held responsible for the tertiary creep stages. The oxidation on the surface and around the graphite nodules was explicitly studied. Layered oxides were identified by combining EDX data with thermodynamic calculations.

Both D5S and HK30 were CL tested at 750 °C, reflecting a higher service temperature of these materials compared with SiMo51. After prolonged creep exposure, HK30 exhibited typical creep cavitation at the grain boundaries, precipitation of sigma phase and G phase, oxide intrusions and recrystallization in a thin layer at the specimen surface. D5S exhibited various types of cavities/voids around the graphite nodules (like SiMo51 at 700 °C) and fracture occurred by shear cracks growing nodule-to-nodule. Various precipitates developed during creep.

Keywords: Creep, creep behaviour, creep damage, ductile cast iron, high-alloyed austenitic cast steel, thermal cycling, tensile testing, stress relaxation, oxidation, precipitation.

Contents

1. Introduction	5
1.1. Development of exhaust manifold materials	6
1.1.1. SiMo51	7
1.1.2. SiMo1000	7
1.1.3. D5S	8
1.1.4. HK30	9
2. Objectives	10
3. Theory	11
3.1 The origin of creep	11
3.2. Constant-load creep tests and creep curves	11
3.3. Five-power-law creep	13
3.4. Creep mechanisms, cavitation and rupture	14
3.5 Cyclic creep	16
3.6. Creep and tensile testing of ductile cast iron	16
3.7. Oxidation of Fe, Fe-Si and Fe-C-Si-Mo (SiMo51)	17
3.8. SRTC (stress relaxations with thermal cycling)	18
3.9. STT (sequential tensile testing)	20
4. Experiments	21
4.1. Specimen preparation	21
4.2. SRTC (stress relaxations with thermal cycling)	22
4.2.1. Temperature Gradient	23
4.2.2. Extensometer measurements	24
4.3. Sequential tensile test (STT)	27
4.4. Constant-load (CL) creep test	28
4.5. Regular, “non-sequential”, tensile tests	29
4.6. Oxidation tests	29
4.7 EBSD	29
5. Results and discussion	30
5.1. Mechanical response to thermal cycling	30
5.2. Comparing stress relaxations with thermal cycling (SRTC), sequential tensile tests (STT) and constant-load (CL) creep tests	31
5.3. Creep of SiMo51 at 700 °C, focusing on “Two-stage” tertiary creep	34
5.4. Creep behaviour and damage of HK30 at 750 °C	37
5.5. Creep behaviour and damage of D5S at 750 °C	39
6. Summary	43
7. Conclusions	44
8. Sustainability statement	44
9. Acknowledgements	45
10. References	46

1. Introduction

Exhaust manifolds (see Fig. 1) are located in the beginning of the exhaust system of truck engines. They collect the hot exhaust gas, flowing from the six or eight cylinders, and pass it further along the exhaust system. Due to starts and stops of the engine, they become subjected to thermal cycling during service. Since they are more or less locked to other components, not allowed to expand or contract freely, stresses arise. To prevent failure, they are usually designed in a way to reduce both stresses and strains in critical sections. In reality, the highest stresses and strains usually arise at sharp transitions, i.e. sudden variations in thickness (and thermal expansion). To avoid this, a “streamlined” design is generally desired.

The manifolds are cast in sand molds and regular materials are ductile cast irons and cast stainless steels. The ferritic ductile cast irons are mainly used for diesel engines and the austenitic cast steels for more demanding applications, e.g. the gasoline engine (otto-engine). D5S may work for both types. The ferritic ductile cast irons are not traditional high temperature materials and have to be spiced and processed in a special way to obtain the required properties. For example, in the case of SiMo51, Si and Mo have been added to give additional oxidation resistance and strength. In addition, the casting process is often simulated beforehand, testing various geometries and configurations to get the desired microstructure and properties.

Firstly, the materials are subjected to mechanical and thermal loads. The service condition described above, involving thermal cycling of locked parts, is usually called thermo-mechanical fatigue. It involves both thermal and mechanical loading – in cycles. Depending on the location, the relationship between stress, strain and temperature differs. It is called TMF-OP when the loading and temperature are Out of Phase and TMF-IP when they are In Phase. For example, the inner surface of a manifold is compressed (-) when heated (+) since thermal expansion is restricted by the cold area of the outer wall. Thus, there is a phase shift of 180° between stress and temperature which is a clear case of TMF-OP. Due to the frequency and lifetime of the thermal cycles in manifolds, this loading is usually associated with LCF (low-cycle fatigue). HCF (high-cycle fatigue) is also present and originates from vibrations from the road and other components. TMF-testing of ductile cast iron, and sometimes with the effect of adding HCF signals, have been thoroughly described in several studies ([1], [2], [3], [4]).

Secondly, the manifolds are oxidized during service, both by hot exhaust gases on the inside and by air on the outside. Most obviously, oxidation decreases the metallic area and may therefore increase the stress. This is, however, not so trivial as the oxides are known to have different load-carrying abilities. Another aspect is that of crack growth: it is well known that an oxide may initiate for instance fatigue cracks but less well known that it may also have a blunting effect on crack tips which may reduce stress concentrations. However, in spite of these “dual” effects, oxidation is generally considered to do bad. In the context of exhaust manifold materials, the effect of oxidation on fatigue has been studied in depth by Ekström [5], and Xiang et al. ([6], [7], [8], [9], [10]), among others.

Thirdly, and central for this thesis, is the creep deformation associated with the thermal cycling. Creep is both a repair and damage process as it unloads the material but also leads to

strain (geometry change) and creep damage. The unloading is due to the transformation of elastic strains into plastic strains, leading to a stress relaxation. Traditionally, creep damage is associated with various sorts of cavitation at grain boundaries and their linkage into cracks. As will be demonstrated, the situation is slightly different for the cast irons due to the occurrence of big graphite nodules in the matrix. Besides the work of the present study, creep of ductile cast irons has for instance been studied by Hug et al. [11].

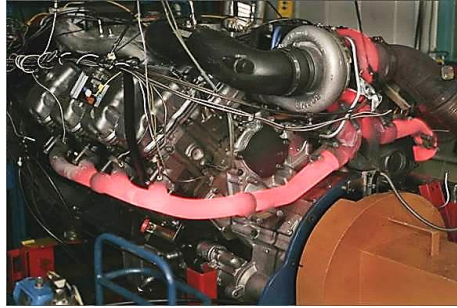


Fig. 1. Exhaust manifold in service (in an engine test cell).

1.1. Development of exhaust manifold materials

As mentioned, the materials used for the exhaust manifolds are mainly ductile cast irons and cast steels. Ductile cast irons are generally defined by a carbon content of minimum 2 wt%. The ductile cast irons tested in the present study comprise a ferritic or austenitic matrix, graphite nodules, carbides and/or intermetallics. The graphite phase has a lower density compared to the metal phase and thus prevents shrinkage pores from developing during solidification.

Compared with the cast steels, the ductile cast irons are generally cheaper and easier to cast. The cast steels intended for the application, on the other hand, offer advantages such as higher corrosion resistance and, according to Ekström [5], higher strength at elevated temperatures. Ferritic grades (in general) have higher thermal conductivity and lower thermal expansion, properties which are considered beneficial for the application. Regarding fundamentals of creep, the activation energy of self-diffusion of iron in γ -austenite (310 kJ/mol) is higher compared to Fe in α -ferrite (280 kJ/mol), Cottrell [12]. For instance, Hug et al. [11] referred to this when they observed more severe creep cavitation in a ferritic ductile cast iron compared to an austenitic one.

The chemical compositions of the included materials are listed in Table 1. Since different casting batches were used throughout the study, compositions are given in ranges according to their respective standards. For the specific composition of each batch and the associated experiments, see appendices 1-5.

Table 1. Chemical compositions (wt%, Fe bal.)

Alloy	C	Si	Mn	Ni	Mg	Cr	P	Cu	Mo	Al
SiMo51	3.0-3.5	4.2-4.8	≤ 0.4	≤ 0.1	0.02-0.08	≤ 0.1	≤ 0.05	≤ 0.1	0.8-1.2	-
SiMo1000	3.0-3.9	2.0-3.2	≤ 0.4	≤ 1.0	-	-	-	-	0.5-1.0	2.5-3.9
D5S	≤ 2.0	4.9-6.0	0.5-1.5	35.0-36.0	-	1.5-2.5	≤ 0.08	≤ 0.50	-	-
HK30	0.25-0.35	0.5-2.0	-	19.0-22.0	-	23.0-27.0	≤ 0.04	-	≤ 0.50	-

1.1.1. SiMo51

SiMo51 is probably the most common material for manifolds in diesel engines. It mainly comprises a ferritic matrix, spherical graphite nodules and carbides. A micrograph of SiMo51 is shown in Fig 2, with one of the carbide segments of Fig 2a being highlighted in Fig 2b. All parts of the segment are rich in Mo and some parts are additionally rich also in Si or Ti. Besides these rather large structures, there are also small particles inside the grains, seen as small black dots in Fig 2b. In creep theory, the larger grain boundary carbides are often considered detrimental while small particles of appropriate structure and composition are considered beneficial. The composition and crystal structure(s) of the carbides were not completely verified but, searching elsewhere, Ekström et al. [13] list Mo- and Si-rich M_6C carbides.

The designation SiMo51 reflects the proportion of 5:1 between Si and Mo contents, see Table 1. Si provides increased “fluidity” of the melt during casting, solid solution strengthening and oxidation resistance while Mo gives solid solution strengthening and carbide formation. Oxidation resistance is derived from the formation of a thin, dense SiO_2 barrier layer at elevated temperatures [5], [14].

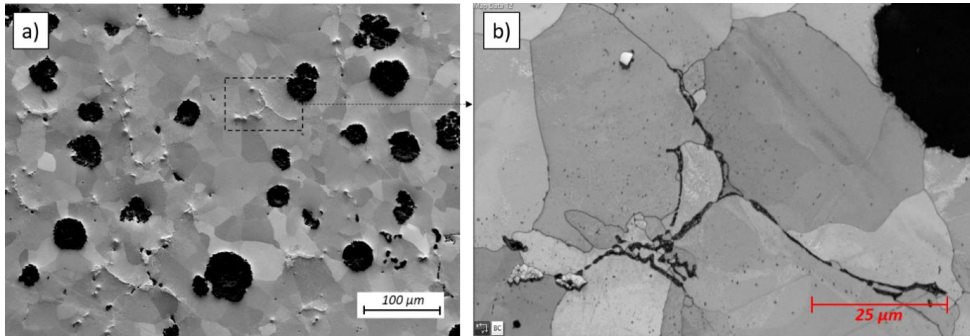


Fig 2. a) FSD (forward scattered diodes) image of the microstructure of SiMo51 and b) EBSD band contrast image of the segment enclosed in a). (From appendix 3).

1.1.2. SiMo1000

SiMo1000 is a ferritic ductile cast iron which is similar to SiMo51 and is also used mainly for diesel engines. It also contains Mo-rich carbides at the grain boundaries and smaller precipitations inside the grains, see Fig 3. Differences are that it contains both spherical and vermicular graphite and has a relatively high aluminium content of about 3 wt% (see Table 1) which adds solid solution strengthening and changes the oxide barrier composition from SiO_2 to Al_2O_3 , see appendix 1. SiMo1000 is marketed as an improved version of earlier SiMo-grades with better oxidation resistance, increased high-temperature strength and also a higher ferrite-to-austenite transformation temperature [15]. It is also marketed as a cheaper alternative to the austenitic D5S. The manufacturer and inventor, Georg Fischer Ltd, recommends usage for applications such as turbocharger housings and exhaust manifolds [15].

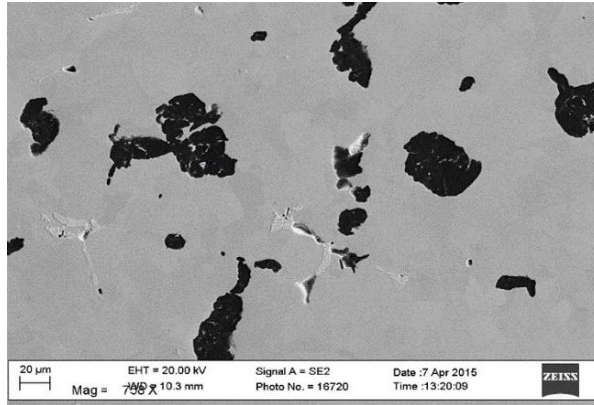


Fig 3. Microstructure of SiMo1000.

1.1.3. D5S

Both regarding price and properties, the austenitic cast iron D5S is somewhere in between the cheap, weak ferritic ductile cast irons (e.g. SiMo51, SiMo1000) and the expensive, strong, oxidation-resistant, cast steels (e.g. HK30). The higher price is mainly due to the high Ni content (≈ 34 wt%) which promotes formation of an austenitic matrix. D5S belongs to the Ni-resist family which includes both flake and spheroidal (referring to graphite shape) cast iron. The etched microstructure, taken from appendix 5, is shown in Fig 4. Casting shrinkage porosities can be seen in a), graphite and mixed structures in b), and a close-up of a mixed structure in c). The latter are “mixed” as they contain several phases, likely both intermetallics and carbides. Unfortunately, they could not be fully identified using quantitative EDX or EBSD, but EDX mapping showed that carbon rich areas are also rich in Cr and that the intermetallics are rich in Si, Ni and, in some areas, also in Mn.

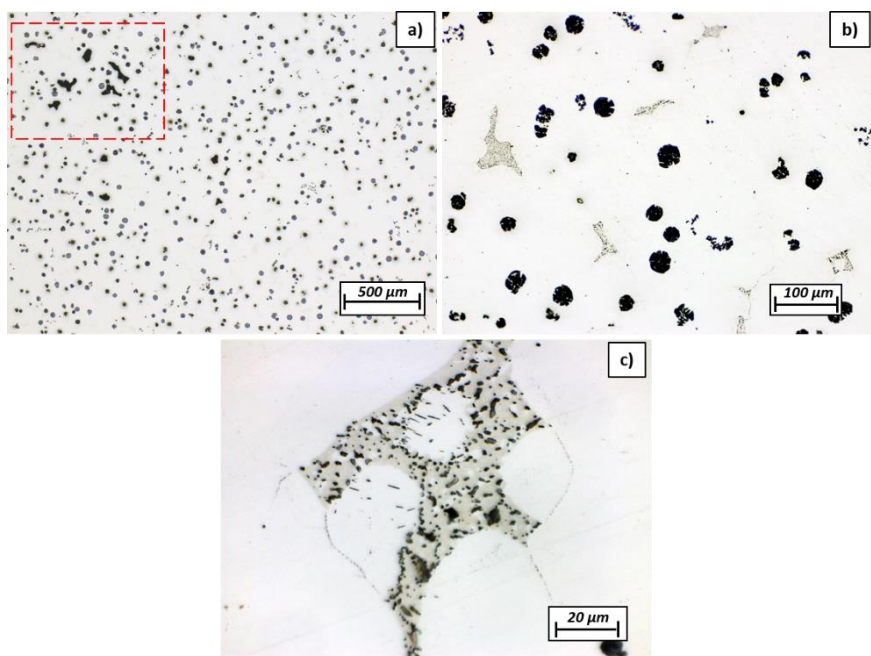


Fig 4. a) Microstructure of D5S (shrinkage porosities are enclosed in red), b) higher magnification, and c) a “mixed structure”. Electrochemically etched by applying 1.5V for about 10s in 5 % HCl in ethanol. (From appendix 5).

1.1.4. HK30

As mentioned, HK30 can also be used for more demanding applications, e.g. gasoline engines. A high Cr-content provides solid solution strengthening and precipitation strengthening by carbide formation, and oxidation resistance through the formation of a thin Cr-oxide film. A high Ni content promotes an austenitic matrix and also provides solid solution strengthening. Compared with more common steels, such as austenitic 304 or 316 steels, the carbon content of HK30 is much higher (0.25-0.35 wt%). According to Piekarski et al. [16], this is beneficial as all Cr is consumed in early formation of carbides and therefore not available to form Cr-rich sigma phase. Sigma phase precipitation is generally considered as detrimental for both mechanical and corrosive properties, but the true effect is complicated and very much case-dependent (see literature review of appendix 4).

In the as-cast and subsequently heat-treated state, HK30 comprises an austenitic matrix and $M_{23}C_6$ carbides, see Fig. 5 (from appendix 4). The carbides occur both as relatively thick particles at the grain boundaries and as small dispersions inside the grains. The orientation map of creep tested material in Fig 6 shows that one of the grains (i.e. dendrites) is at least 11 mm across. Since the creep specimens have a diameter of 10 mm, creep test results will inevitably reflect properties close to those of a single crystal. There is very limited creep data on HK30 available but there is more on HK40 (25Cr-20Ni-0.4C) which has a higher carbon content of 0.4 wt%. For instance, HK40 has been studied with regard to creep by Whittaker et al. [17] and Konosu et al. [18].

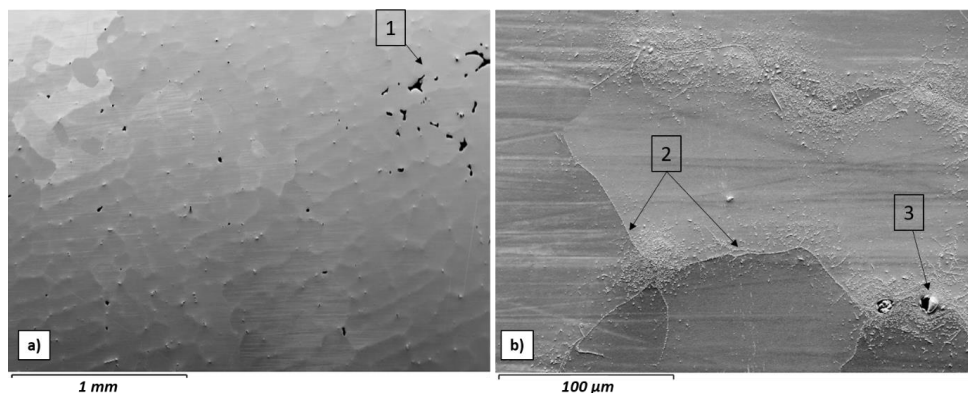


Fig. 5. a) Microstructure of HK30. (1) points towards an area of shrinkage porosities. b) segregation boundaries. (2) points towards M₂₃C₆ carbides and (3) towards a TiN-particle. Images from appendix 4.

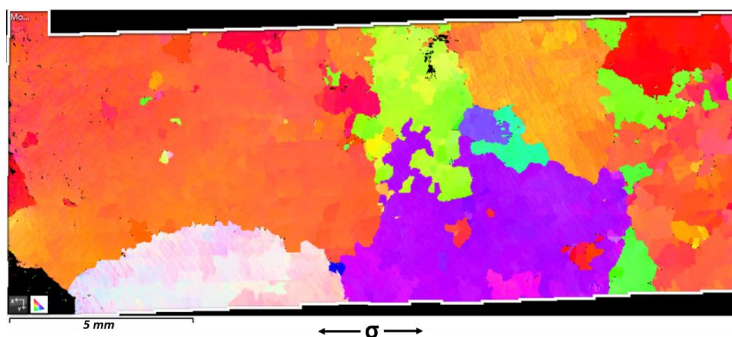


Fig 6. Orientation map of creep tested HK30 material. (59 MPa, 750 °C). Images from appendix 4.

2. Objectives

The primary objective of the present thesis is to investigate creep behaviour of the included cast materials, both in terms of creep parameters/curve characteristics and creep damage. Since the ductile cast irons, SiMo51 and SiMo1000, have big graphite nodules and oxidize rather heavily, the creep response is expected to be different from that of pure metals as well as more traditional high-temperature materials, e.g. Ni-base superalloys, and highly alloyed steels. HK30 is similar to such “super grades” in several respects but the casting defects and the coarse-grained structure make it unpredictable. The austenitic ductile cast iron D5S is interesting as it lies somewhere in between the SiMo-materials and HK30. It includes large graphite nodules but also comprises a highly alloyed austenitic matrix.

The investigated grades are used in various types of exhaust truck engines all over the world and are constantly exposed to creep – but have barely been creep tested. There may be several reasons for this:

- i) Service temperatures have steadily increased with engine development, implying a gradually increasing contribution from creep deformation. Thus, creep may not have been that critical in the past.
- ii) Compared with regular tensile tests, constant-load creep tests are more complicated, much more expensive, and generally more time-consuming (obviously depending on load and temperature). Additionally, since they are not controlled by deformation rate, it is more difficult to estimate times to rupture in constant-load creep tests and thus to select suitable loads.
- iii) Large steel companies have financed creep testing of processed steel. The foundries are often operated by relatively small companies with less resources to finance such research.
- iv) Cyclic creep, which is the case of manifolds, has perhaps been considered too complicated to account for.

As a second objective of the thesis, connecting with ii) and iv), attempts have been made to compare faster methods, more specifically cyclic stress relaxations and monotonic, sequential tensile testing, with the monotonic constant-load creep test method.

3. Theory

3.1 The origin of creep

Creep refers to slow, time-dependent plastic deformation at high temperature, usually starting at around half of the melting temperature. As stated by Kassner [19], creep is enabled due to a decrease in yield stress, derived both from high temperature and low deformation rate.

The temperature dependence arises since atomic motion is assisted by vibrations and because the atoms are able to climb and diffuse around obstacles, Manson and Halford [20]. Another effect is that the atomic bonds are longer and weaker at higher temperatures.

The strain-rate dependence can be explained by the smaller force required to move atoms slowly [21], explaining why creep is considered a “below the yield stress” phenomenon. As exemplified by Manson and Halford [20], the yield stress obtained in a slow tensile test of, for instance, 10^{-7} s^{-1} , is often much lower compared to the “conventional” yield stress which is obtained in a regular tensile test ($\approx 10^{-4} \text{ s}^{-1}$).

3.2. Constant-load creep tests and creep curves

Constant-load creep testing is the conventional way of testing creep. Regarding control parameters, it is quite simple since the load is kept constant at constant temperature, throughout the whole test. The general trends with stress are illustrated by three curves in Fig 7. The four main segments of a creep curve (1-4) have been indicated in the case of the lowest stress, σ_1 .

(1) marks the initial loading, seen as a vertical shift of each creep curve.

(2) marks the primary creep regime, characterized by an increase in dislocation density and a resulting decrease in creep rate.

In the secondary creep regime (3), the deformation hardening in (2) is balanced by dislocation annihilation, i.e. recovery, resulting in a constant strain rate. For this regime to develop, it is also necessary that the microstructure is stable. The secondary creep regime is, however, an ideal case. In real life creep testing, the strain rate is seldom, or in very rare cases, completely constant as some type of “damage” sets in and give at least a slight increase in strain rate [22].

Finally, (4) marks the tertiary regime in which accumulated creep damage, crack growth and a reduced load-carrying area accelerate deformation to the point of creep rupture, often indicated by an ‘x’.

A lower stress (σ_1) usually leads to a longer secondary creep (in time), a longer time to rupture and a low strain to rupture [19]. The time and strain to rupture are naturally related: longer times usually mean more evolved creep cavitation and a more brittle fracture, with only small elongation upon rupture. Correspondingly, relatively high stresses (σ_3) mean negligible or shorter secondary creep, less evolved creep cavitation and a more ductile fracture. Regular characteristics are then: large strain-induced voids, shear cracks, necking and high strain to rupture [23].

In order to better understand the sequence of events during a creep test, creep strain *rates* are usually plotted, either as a function of time or of strain, see illustration in Fig 8. The creep strain-rate curves observed in the present study can be explained by general dislocation and/or crack theories. The trends are again illustrated by three curves, one for each stress, see Fig 8. For each curve, the red marker illustrates the lowest value of strain rate. If the strain rate stays on this level, it is called the “steady-state” creep rate. If it instead shows an inflection point, i.e. a direct transition, the rate is simply referred to as the “minimum creep rate”. A direct transition is made possible by, for instance, cavitation, early crack growth, oxidation, or in any other way an unstable microstructure. Since complete steady state is more of a theoretical or “ideal” state, the minimum creep rate is usually used when presenting results, for instance in a Norton plot which includes the minimum creep rate and applied stress [22].

The trends illustrated in Fig 8 are, however, valid both in the case of a steady state and in the case of a direct transition. Real plots of strain rate usually have log-10 scale (semi-log or log-log). Regarding vocabulary, “hardening” and “softening” are sometimes used to point towards segments of decreasing and increasing creep rates, respectively.

In the $\dot{\epsilon}$ -t-curve (Fig 8a), the steady state/minimum creep rate is reached earlier for higher stresses. This is quite natural as a high stress generates many dislocations which quickly start annihilating – a requirement for steady state. Additionally, it is natural to have early crack growth, leading to a direct transition. In the case of a lower stress, there is instead a slow deformation hardening, and it takes a long time to build the dislocation density needed for wide-spread annihilation. It also takes longer time for cracking (causing a direct transition) to take place since the creep damage accumulates more slowly.

In the $\dot{\epsilon}$ - ϵ -curve (Fig 8b), the situation is reversed: the steady state/minimum creep rates are generally reached at lower strains for *lower* stresses. A high strain is simply not needed to reach either steady state or cause early cracking – if things are allowed to develop slowly. “Things” include a high dislocation density, leading to a steady state, or cracks, leading to a

direct transition. The general trend that a higher strain is needed to reach steady state if the stress is high is also emphasized by Kassner, see Fig. 5 in [19] (originally published in [24]).

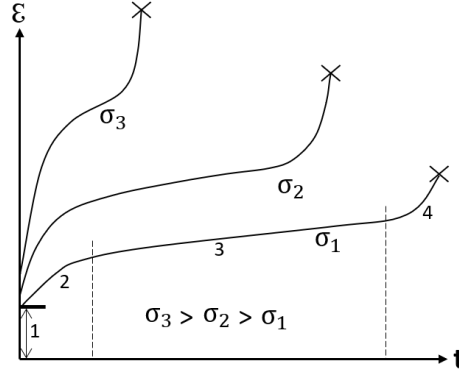


Fig 7. Typical creep curves obtained from a constant-load creep test.

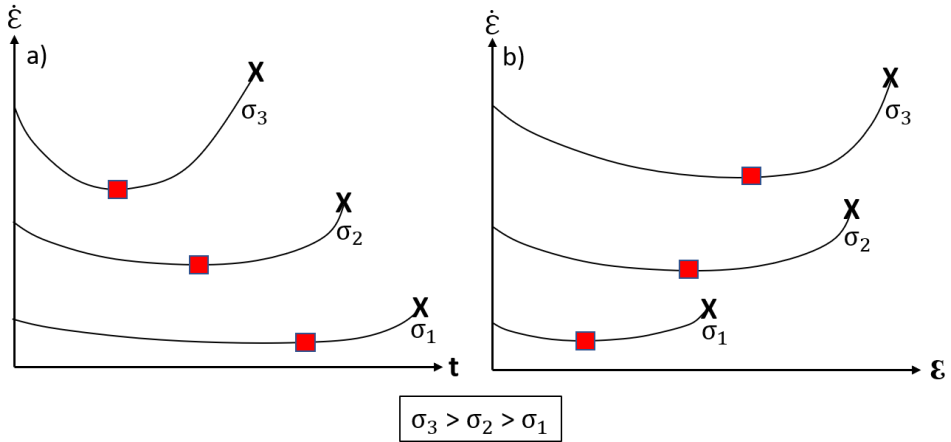


Fig 8. Typical scenario for three stress levels with: Creep strain rate as a function of a) time and b) strain. (x = rupture).

3.3. Five-power-law creep

For most pure metals and many alloys, the “steady-state” creep rate is linked to the applied stress through Norton’s law [25]:

$$\dot{\epsilon}_{ss} = A_0 \exp \left[-Q_C / kT \right] (\sigma_{ss} / E)^n \quad (1)$$

$\dot{\epsilon}_{ss}$ = secondary creep rate, A_0 = constant, Q_C = activation energy for creep, k = the Boltzmann constant, E = Young’s modulus, n = Norton exponent.

As outlined, in real life creep testing we usually present a minimum creep rate as the creep rate is practically never completely constant [22]. Because of the power-law relationship in eq. 1, minimum creep rates are often plotted as a function of stress in double logarithmic,

Norton plots. The slope (n) is basically a measure of how dislocations are created and annihilated in the material. The minimum creep rate is selected as that is the point where dislocations are created and annihilated with the most even rate [22]. For pure metals and many alloys, the slope (n) is then usually around 5. Because of these circumstances, expressions like “five-power-law creep” or simply “power-law creep” are often used. The limit is not very distinct and n -values of about 4-7 fall within five power-law creep [19]. If the n -value is the same over the tested stress range, it indicates that the creep mechanism is constant. A change in n (in any direction) is usually referred to as “power-law breakdown” and indicates that a new creep mechanism becomes predominant.

The microstructural events taking place during creep, referring to the “dislocation” length scale, are well-documented within the range of “five-power-law creep”. When plastic deformation commences, the dislocation density increases and subgrains form. They arise as a low energy geometry of the introduced dislocations and typically give rise to misorientations of around 1° . Inside these subgrains, so-called Frank networks form. These in turn consist of single dislocations, arranged in “criss-cross” substructures [19].

The subgrain boundaries and their movement are often linked to the creep strength of a metal. It is preferred to have a lot of small dispersions inside the grains which “pin” the subgrains, thereby lowering creep rates [26].

3.4. Creep mechanisms, cavitation and rupture

Creep deformation is controlled by various mechanisms which may be more or less active, depending on stress and temperature. The relationships are sometimes presented in Ashby deformation maps, named after their inventor. An illustration is shown in Fig 9. Each of the four regions are associated with a deformation mechanism.

Dislocation creep (2) consists of both dislocation glide and climb where the climb step, often called “recovery”, is a form of diffusion by which entire dislocation segments annihilate each other. Even though the glide step creates almost all of the strain, the climb step sets the rate, and as a result the mechanism is often termed “climb-controlled” [27]. Within five power law creep (see paragraph 3.3) the activation energy of creep (Q_c) has been observed to closely follow that of lattice self-diffusion (Q_{SD}). This has led to the nowadays widely accepted conclusion that creep, within this regime, is climb-controlled (since climb is a form of diffusion) [19].

“Diffusional flow” is usually divided into Coble and Nabarro-Herring creep (3-4). In the case of Coble creep, it refers to a stress-induced flow of matter along grain boundaries, while in Nabarro-Herring creep, it refers to flow by lattice diffusion. Coble creep is more easily activated and occurs at lower temperatures and stresses while Nabarro-Herring is activated at higher temperatures and stresses [27]. As mentioned, creep tests are rarely conducted in these regions as strain and damage evolve too slowly. In this context, it can be pointed out that clear documentations of diffusional flow are rare, and it has only been documented in a few creep studies on steel. This includes work by Nilsson et al. [28] who did constant-load creep tests on austenitic (20Cr, 30Ni, Ti stabilized) steel at 800 °C. They found a distinct transition with a change in Norton exponent from $n=1$ to $n=2.7$ at 5 MPa, which was related to a change from Coble creep to power-law (dislocation based) creep. By TEM-imaging, they could see

that no matrix or twin-boundary dislocations occurred in the case of 3 MPa whereas significant amounts could be found in specimens tested above 5 MPa.

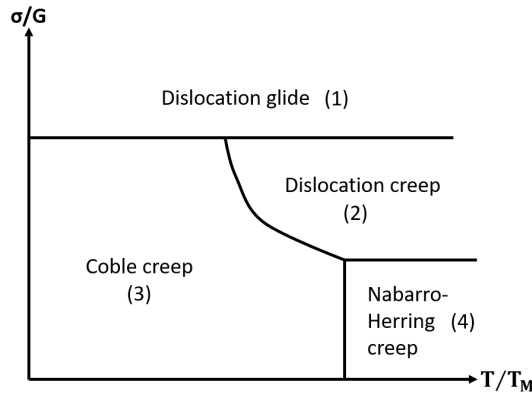


Fig 9. Ashby deformation map

In an extensive review by Ashby et al. [23], the mechanisms of Fig 9 are related to the formation of creep cavities and the subsequent fracture. They point out that ductile fracture at lower temperature is basically controlled by the formation of large, strain induced ovals around inclusions, often followed by intragranular fracture. However, as the temperature is raised, a new type of fracture is viable. Ashby et al. [23] call it “intergranular, creep-controlled fractured”. Under these conditions, grain boundaries start sliding, wedges are initiated, and creep cavities grow under mysterious circumstances. Since grain boundaries typically concentrate stress, they are likely to be found as initiation spots for cavitation.

The mechanism of creep cavity nucleation is widely debated and to this day not verified. However, there are several theories, of which Kassner [19] lists the following: i) grain boundary sliding, ii) vacancy condensation at a high stress interface, iii) dislocation pile-up.

Grain boundary sliding, i), is by some believed to nucleate cavities due to the stress concentrations arising particularly at triple points, although it is debated whether the stresses really are big enough to nucleate cavities. Vacancy condensation, ii), refers to the diffusion-based accumulation of vacancies into cavity “nuclei”. Dislocation pile-up, iii), may readily occur against hard particles and grain boundaries, following a so-called Zener-Stroh mechanism. The theory, reviewed by Kassner [19], suggests that the stress concentrations arising from the pile-ups are sufficient to nucleate cavities.

In the review paper by Ashby et al. [23] another, perhaps related explanation, is also listed. This proposes that cavities are nucleated by pure diffusional flow at stress-concentrating surfaces but later grow in a coupled state. In this mode, pure diffusional flow is active on a local scale around a single cavity but coupled to global areas of power-law “creep cages” which set, or at least influence, the local diffusion rate around the cavity.

3.5 Cyclic creep

Few studies have involved how creep behaviour or creep rates are affected by a reversal of the load. One reason for this may be that most traditional creep test rigs cannot do the reversal from tensile to compressive loading as they use dead weights to load the specimen. In that case, other machines, likely designed for fatigue experiments, are needed. Another may be that compressive creep is not considered an issue since any cracks remain closed. However, for the application of manifolds, creep rates in compression are also of interest to get the net strain after many cycles.

On this topic, Swindeman [29] tested Inconel at 816 °C, comparing monotonic creep tests in tension to cyclic creep tests, using the same (absolute) load values. In the cyclic tests, the load was reversed when the strain reached a desired level, meaning that the test was load-controlled but strain-triggered. Quite remarkably, the obtained times to rupture in monotonic tensile loading were up to 4 times shorter at higher stresses and 2 times shorter at lower stresses compared with the cyclic creep test. From this, Swindeman concluded that the time under tensile loading is critical. He also pointed out the quite obvious: the stress increases in a monotonic tensile test due to a decrease in load-carrying area but essentially remains the same in a cyclic test (if the net strain is controlled to zero). A bit surprising, the measured strain rates were higher in the cyclic creep test (although primary creep accounted for most of it). Manson and Halford [20] explain the matter further by assuming a creep mechanism of grain boundary sliding along the 45°-direction (with respect to load). They suggest that strain rates are higher in tension due to less “friction” between the atoms compared with shear in compression (along the same boundary).

3.6. Creep and tensile testing of ductile cast iron

Creep studies on cast irons are quite scarce, but a few were found. For example, Martinsson et al. [30] tested a ductile cast iron at 100 and 125° up to 41,000 h. The material was tested for the purpose of nuclear waste storage, or more specifically the supporting frame of the copper canisters used to store the waste fuel. Results showed logarithmic creep, i.e. creep rates which after some time barely could be measured. A closer microscopical investigation showed no creep cavitation.

Being more relevant for the present study, Hug et al. [11] constant load tested three ductile cast irons, two ferritic and one austenitic, between 650 and 900 °C. The presented creep curves showed small primary creep followed by small or negligible secondary creep and dominating tertiary creep. Quite remarkably, all data could be fitted to one Monkman Grant line, indicating one common creep mechanism for ferritic and austenitic cast irons. The damage was reported as plastic flow of the matrix in the high stress/short-time specimens and diffusion-based cavitation in the low stress/long-term specimens. Oxidation was also observed, but the layers were reportedly too thin to have a significant effect on creep.

The deformation behaviour of ductile cast iron has been extensively tested - using high deformation rates. In a study by Hervás et al. [31], ferritic SiMo cast iron was tested under tensile and compressive loading at temperatures up to 800 °C. Up to 400 °C, the tensile test curves showed deformation hardening which was, however, replaced by efficient recovery above a test temperature of 500 °C. In tension, at 400 °C and below, damage was reported as plastic deformation and cracking of the nodules. The nodules were also damaged through an

“onion-like” mechanism. In this case, the outer shell, obtained by solid state diffusion during solidification, was peeled off from the inner core (which is formed directly from the melt). At higher temperatures, above 400 °C, there was significant plastic flow of the ferritic matrix, even more pronounced void formation around nodules and a higher strain to rupture. In compression, below 400°C, damage was reportedly plastic flow of the ferritic matrix and fractured nodules at high strains. Above 400 °C, plastic flow was reported, but neither cracks nor voids could be observed.

The significance of graphite nodules for plastic properties has been discussed in several studies. For example, Sjögren et al. [32] tested flake and compacted cast iron and suggest micro-yielding in the vicinity of graphite particles. They similarly suggest that higher stresses lead to void formation at the graphite-matrix interface.

Furthermore, Dong et al. [33] did in-situ observations as they tensile tested a ferritic ductile cast iron directly inside the SEM. They could see the following stages of deformation: 1) slip-lines in the elastic regime, 2) small decohesion at the graphite-matrix interface right after exceeding the macroscopic yield stress, 3) large ellipsoidal voids around graphite nodules, 4) fracture by shear cracks, linking the voids together, 5). In their modelling of the tensile test curves, which reportedly was successful, they assumed a porous material in which the graphite nodules were simply replaced by voids. The assumption was supported by the observation that voids develop at the matrix-graphite interface immediately upon yielding (2) without any “resistance” from the nodules.

3.7. Oxidation of Fe, Fe-Si and Fe-C-Si-Mo (SiMo51)

If oxidation is severe, it may influence creep both regarding crack growth and decrease in load-carrying area. In any of these cases, the effect of oxidation on the registered creep strain values can be considered and compared with other effects such as creep damage growth and reduction of load-carrying area due to pure straining. Of the materials included in the present study, the three cast irons SiMo51, SiMo1000 and D5S were prone to oxidize heavily compared to the cast steel, HK30. Especially in CL-testing of SiMo51 at 700 °C, oxidation was pronounced with a mean thickness of about 500 µm (10 % of the original specimen radius) along the gauge of the most prolonged specimen (339 days at 12 MPa). (However, as described more detailed in appendix 3, only half of the oxide was estimated to reduce the metallic area).

The theory surrounding oxidation of metals states that oxidation occurs outwards from the base metal due to migration of metal ions towards air, and inwards due to migration of oxygen ions towards the base metal [5]. For stoichiometric reasons, scales of FeO, Fe₃O₄ and Fe₂O₃ form when pure iron oxidises (ordered from the base metal to air).

The addition of Si to Fe is interesting as SiMo51 is included in the present study. Although addition of Si also has other effects, for instance on casting and strength properties, the main reason is often to obtain a barrier of SiO₂ during service at high temperatures. As it is generally dense and uniform, such a scale has the ability to effectively prevent further oxidation. Since oxide growth generally slows down by time due to protection from existing scales, growth rates tend to follow a logarithmic relationship with time. By adding Si, this effect becomes even stronger. Another situation, not desired, is when the oxides spall off, continuously refreshing the exposure of metallic surface to air. This is common, in for

instance TMF-cycling, where the difference in thermal expansion and plastic properties between oxide and metal sometimes leads to spallation, i.e. oxides “jumping” off the surface.

Regarding pure Fe-Si alloys, Liu et al. [34] oxidation tested three grades of 2.75, 4.97 and 6.96 wt% Si. As the 4.97 wt% Si grade (close to SiMo51 in Si content) was exposed at 700°C for 24h, a thin, covering Si-oxide formed together with “oxide nodules”. The nodules included Fe₂O₃, growing outwards from the base metal, and Fe₃O₄, growing inwards, mixed iron and Si oxides and, innermost, a thick Si-rich internal oxidation layer, also containing SiO₂ particles.

In the even more specific case of SiMo cast iron, Ekström et al. [13] did oxidation tests of SiMo51 at 700 and 800 °C, observing Fe-oxides growing around graphite nodules and carbides followed by “island growth” (similar to “oxide nodules”). The more uniform scale, obtained after “steady-state”, consisted of layers of Fe₂O₃ and Fe₃O₄, both growing outwards, and layers of Fe₃O₄, spinel and SiO₂, growing inwards.

Ebel et al. [14] also did oxidation tests of a SiMo ductile cast iron, at 700 and 800 °C. Similarly, two outwards growing layers of Fe₂O₃ and Fe₃O₄, and two inwards growing layers of Fe₃O₄ and Fe₂SiO₄ were observed. The outwards growing layers were reportedly filled with porosities while the inward growing oxides contained trace marks of old spheroids.

3.8. SRTC (stress relaxations with thermal cycling)

This type of test starts by heating of a typical tensile test specimen under zero load (continuous unloading) to a desired start temperature, also acting as the lower limit of the thermal cycling test. From then on, the machine is instructed to keep the position of the movable grip completely still, thereby locking the specimen in its full length (in the present case the lower grip was locked as the upper grip is always fixed). This condition is active throughout the whole test without interruption.

Following this instruction, the specimen is thermally cycled between the lower and upper temperature limits. Since the specimen is locked, heating results in a compressive stress while cooling leads to a tensile stress. Between heating and cooling, there are hold times of constant temperature. If the hold time temperatures and stresses are high enough, there are stress relaxations arising from creep. See example of HK30, cycled between 700 and 800 °C (Fig 10). In each reversal, the stress builds up until the yield stress is reached. Since the yield stress was often reached during the ramps, before the hold times, the hold time was generally preceded by some pre-deformation. Only this hold time data, with accompanying stress relaxation, were compared to data obtained by the two other methods (STT and constant-load creep-testing).

Interpretation of results is complicated as the measured strain includes thermal, elastic and plastic contributions. Thermal and elastic strains directly follow temperature and stress. Plastic strains include plastic flow and creep strain, the former by pure dislocation glide and the latter by some creep mechanism (e.g. dislocation creep). The contributions from elastic, thermal and plastic strains could be varied by changing the settings of the thermal cycle, i.e. the temperature limits and/or the heating/cooling rates or hold times.

The creep rates during hold times could be obtained by first calculating the true strain, this is plotted in Fig 10, and then removing the elastic strain contribution, $(\frac{\sigma}{E})$, to obtain the plastic strain.

After the true plastic strain had been obtained, the data was standardized in order to facilitate curve fitting of the strain evolution during the hold times, a procedure which is described more detailed in appendix 2.

The following function, combining a linear and exponential relationship, was used for curve fitting of (standardized) strain evolution with time:

$$y_s = p_1 + p_2 \cdot x_s + p_3 \cdot \exp(p_4 \cdot x_s)$$

The standardized experimental time, t_s , and standardized experimental strain, ε_s , were used to evaluate p_1 to p_4 by minimizing the error of:

$$(x_s, y_s) = (t_s, \varepsilon_s)$$

during a relaxation. The modelled strain vs. time was obtained by reverting the standardization procedure:

$$x_s = \frac{x - \bar{x}}{\text{std}(x)}$$

$$y_s = \frac{y - \bar{y}}{\text{std}(y)}$$

where \bar{x} and \bar{y} represent the average values and std defines the standard deviation.

The corresponding strain rate during relaxation was calculated from:

$$\dot{\varepsilon} = \frac{d\varepsilon}{dt} = \frac{dy}{dx} = \frac{\text{std}(y)}{\text{std}(x)} \cdot \frac{dy_s}{dx_s} = \frac{\text{std}(y)}{\text{std}(x)} \{p_2 + p_3 p_4 \cdot \exp(p_4 \cdot x_s)\}$$

The same function of y_s was used to fit the stress relaxation data (during hold times) which, as can be seen in Fig 10, follow a similar evolution with time. This curve fitting was necessary for removing scattering in the stress evolution during relaxation, mainly arising from temperature fluctuations which are directly converted to stress fluctuations in the locked specimen.

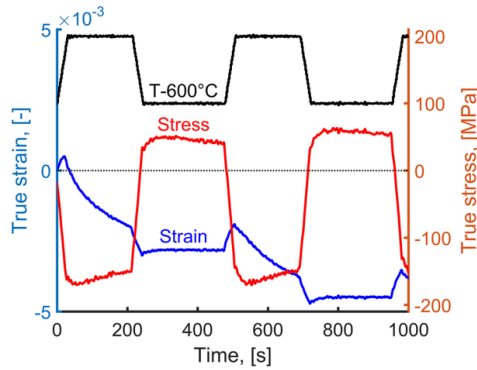


Fig 10. Cycling of HK30 between 700 and 800 °C by

heating/cooling rates of 200 °C/min and hold times of 3 min. The temperature is indicated on the stress axis and has been vertically shifted by 600 °C.

3.9. STT (sequential tensile testing)

In the present study, sequential tensile tests (STT:s) were carried out to see if the results agreed with, or in any way could be related to those obtained from traditional constant-load creep tests. The meaning of “sequential” is that the strain rate is changed multiple times in sequences over the strain range of one single tensile test. Each time, the applied strain rate results in a “saturation stress”, ideally also corresponding to “steady-state”. Thus, this is a direct way of testing strain-rate sensitivity. A fundamental difference between the methods is the control parameter: tensile tests are controlled by strain rate and creep tests by load. But is there any difference in the output? Kassner [19], who instead calls the test a “strain-rate increase” test, points out that the saturation stress obtained in a tensile test can be treated as steady state if it has been reached due to a balance between hardening and dynamic recovery processes. However, Kassner adds that the stress at which there is constant dislocation structure is often “ambiguous”. Another complication, discussed in appendix 2, is that deformation hardening taking place in sequences of high strain rate affect the following sequences of the test due to deformation hardening. To sum up, there is a lot to consider when comparing the constant-load creep tests and tensile tests.

The same procedure was used for all STTs in the present study. As described, the test is controlled by strain rate but there are trigger points at certain strain levels where the strain rate is changed. In the first sequence (0-2 % strain), a high strain rate of 10^{-4} s^{-1} is set. The strain rate is then lowered in steps (2-4) down to 10^{-7} s^{-1} followed by a new increase each 0.5 % of new strain up to $3.3 \cdot 10^{-3} \text{ s}^{-1}$. See Table 2 and Fig 11. It can be noted that the test routine is designed to evenly distribute data in a logarithmic diagram. The resulting Norton plots of each test may include more or fewer than eight points, for instance due to early fracture (below 5.5 % strain) or oscillations in stress or strain rate leading to discarding points or letting two values from the same segment indicate the spread. In the past, Appelt [35] has used the very same STT method (and equipment).

Table 2. Order of sequences in STT.

Sequence	1	2	3	4	5	6	7	8
ϵ [-]	0.000-0.020	0.020-0.025	0.025-0.030	0.030-0.035	0.035-0.040	0.040-0.045	0.045-0.050	0.050-0.055
$\dot{\epsilon}$ [s^{-1}]	10^{-4}	10^{-5}	10^{-6}	10^{-7}	$3.3 \cdot 10^{-6}$	$3.3 \cdot 10^{-5}$	$3.3 \cdot 10^{-4}$	$3.3 \cdot 10^{-3}$

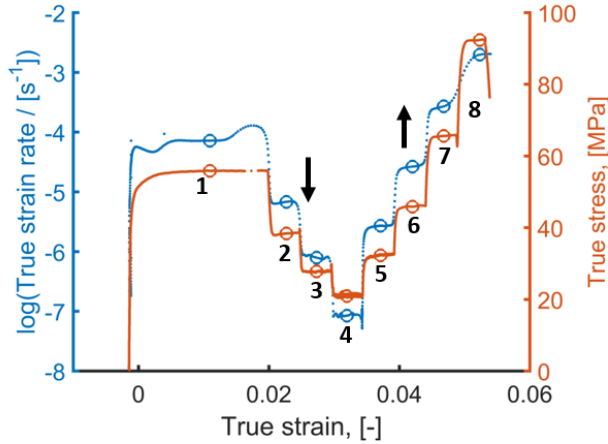


Fig 11. STT test of SiMo51 at 700 °C.

4. Experiments

4.1. Specimen preparation

Specimens were manufactured from cast plates, see Fig 12a. In order to avoid casting defects, the plates were cast in connection to large cylinders which were cut off and thrown away. Only the mid-section was used for manufacturing of test specimens, as indicated by the schematic test specimen added to the illustrated in a). Various foundries were involved: HK30 material was cast by Smålands gjuteri AB, Eksjö, Sweden, SiMo51 material by Castings P.L.C, West Midlands, England, SiMo1000 by Georg Fischer Eisenguss GmbH, Herzogenburg, Austria and D5S by Josef Brechmann GmbH & Co, Germany.

Specimen geometries are shown in Fig 12: b) CL, c) STT and d) tensile test specimens (used for both SRTC and regular tensile testing).

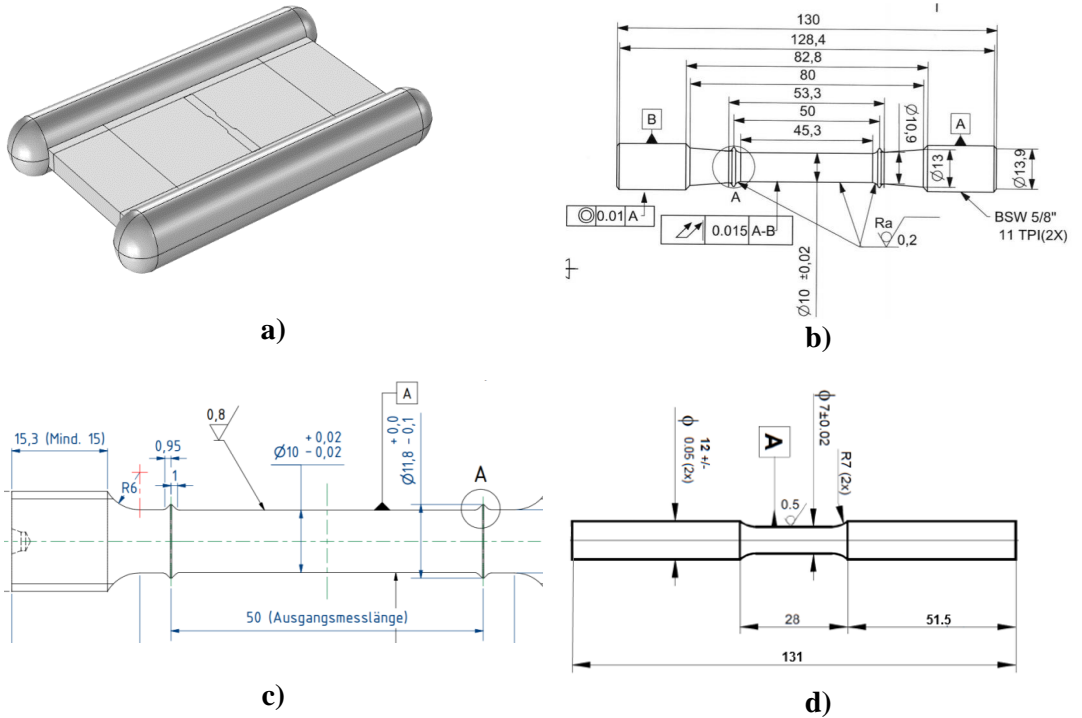
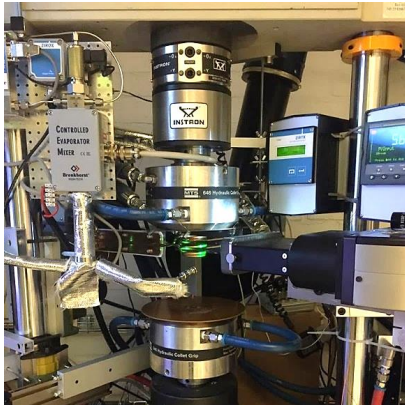


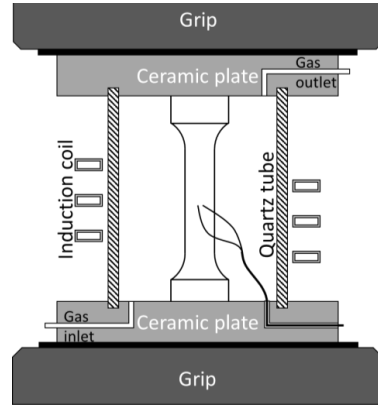
Fig 12. Geometries of a) Cast plates and specimens used for b) CL, c) STT and d) SRTC and tensile tests.

4.2. SRTC (stress relaxations with thermal cycling)

A test rig with a 100 kN alignment fixture, a 25 kN Instron load cell, water-cooled grips and an EDC-580 V Doli control system were attached to a load frame which was originally intended for an Instron 8561 machine, see Fig 13. An induction system of 5kW (by Teknoheat AB) and an induction coil of copper is used for heating. There are two possible options of measuring strain: by a laser extensometer, relying upon speckle pattern tracking (Laser Xtens compact TZ, Zwick Roell), or by a contact extensometer with aluminum-oxide pins (MTS 632.53F-14). A few tests were also conducted in inert atmosphere, see appendix 1. For that practice, a gas-tight chamber setup, developed by Ekström [5], was used, see Fig 13b. Thermocouples of S-type were spot-welded to the surface, following the TMF validated code of practice of a small distance (<1 mm) between the two weld points [36].



a)



b)

Fig 13. a) Test rig used for SRTC and b) air-proof chamber.

4.2.1. Temperature Gradient

Compared with a furnace, a clear disadvantage of using induction heating is the inevitable temperature gradient developed in the test specimens. The gradient is for instance affected by convection, thermal and electrical conductance and radiation, as well as any magnetic transition. Since experiments involving thermal cycling were conducted (SRTC), the gradient and its possible effects on the results had to be elucidated. Fig 14 shows results from a measurement of the gradient using the ferritic ductile cast iron SiMo51, involving three thermocouples which were welded 5 mm below, right at, and 5 mm above the middle of the gauge length. The middle thermocouple was used for control and thus shows the set temperature in distinct ramps.

As can be seen in Fig 14, the gradient increases steadily as the temperature is raised. This is related to heat conductance; the temperature difference between the hot zone and the surroundings becomes larger and larger with the grips of the test rig acting as heating sinks, Verma et al. [37].

At about 700 °C, the Curie temperature is reached. This marks a magnetic transition from ferromagnetic (always magnetic with internal magnetic domains) to paramagnetic (magnetic only in the presence of an external field). At this point, the gradient instantly becomes almost zero. Verma et al. [37] explains that in the ferromagnetic range, both joule and hysteresis heating are active. Joule heating is caused by the eddy currents generated by the alternating magnetic field and “hysteresis” refers to heat generated from magnetic hysteresis losses. In the paramagnetic state, hysteresis heating vanishes, and an extra energy input is needed to continue heating the specimen at the same rate. From this, see Fig 14, it appears very likely that the point of the middle thermocouple first becomes paramagnetic, leading to an increase in effect (the energy input) which increases the temperatures in the surrounding, still ferromagnetic parts of the gauge, quickly pushing the gradient to almost zero. With this result in mind, the effect on thermal cycling tests (e.g. SRTC) is that the strains measured by the contact extensometer ($L_0=12$ mm) are less accurate at lower hold temperatures, below the Curie temperature. That is, when the extensometer pins are pressing against colder areas than what is given by the control thermocouple, strains in the very middle will be underestimated as the measurement length of 12 mm in that case is too long. At temperatures above the Curie

temperature, the more homogenous temperature leads to more homogenous deformation along the measurement zone, and measurements are more precise.

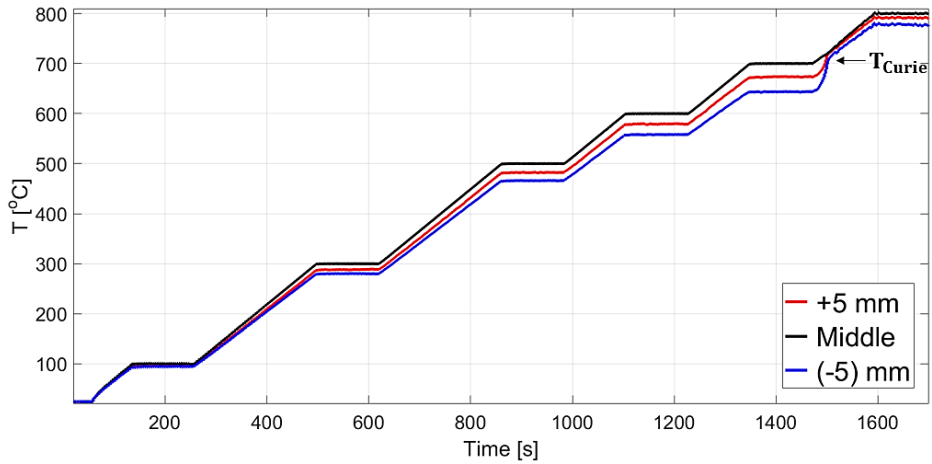


Fig 14. Temperature recorded 5 mm above, at, and 5 mm below the middle of the gauge length.

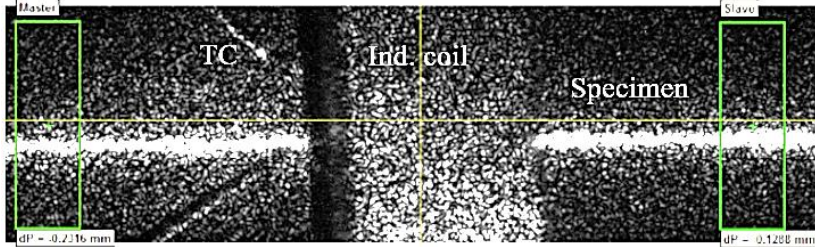
4.2.2. Extensometer measurements

As mentioned, it was possible to do the SRTC tests using either a contact or laser extensometer. In appendix 1, the laser extensometer was used, while in appendix 2, the contact extensometer was used. It was found that the two devices generally show the same strain evolution, i.e. the same strain curve characteristics, but that the signals differ in *strain level* (by several factors).

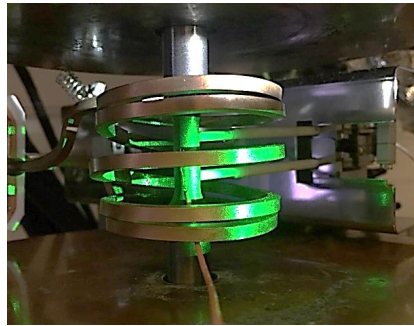
Fig 15a shows a specimen lying horizontally, with the two ends of the thermocouple (TC) having a weld point below the middle winding of the induction coil (Ind. coil). L_0 , the measurement length, is set by changing the distance between the two green boxes of master and slave. The strain measurement relies upon surface pattern tracking; as the laser light hits the specimen surface, a speckle pattern forms based on the scattering angles of the laser light. During a test, the individual speckle patterns in the master and slave boxes are tracked by a video camera and the distance between them is converted to a strain.

Clear advantages using this quite novel measurement technique are non-existing preparation times and a low risk of damaging the specimen or extensometer device.

The contact extensometer, see Fig 15b, measures the strain as the distance between two pins of aluminium oxide, pressed onto the specimen surface. It has a fixed measurement length, in this case of $L_0 = 12$ mm. An advantage is the matter of trust: this type of device has been used for a long time and has a good track record. A clear disadvantage is the physical contact point between the pins and the specimen which may initiate cracks.



a) Tracking of speckle patterns using the laser extensometer. The green tracking boxes, thermocouple (TC), induction coil and specimen are shown in a horizontal view. Arrows indicate the axial direction of the specimen. The weld point of the TC is below the middle winding of the induction coil marked Ind. coil (where the two TC wires meet).



b) Strain measurement using the contact- and laser extensometers simultaneously.

Fig 15.

To validate the performance and compare results between the two extensometers, a test was carried out using both of them simultaneously, see experimental setup in Fig 15b, above. HK30 was SRTC-tested with a lower and an upper limit of 500 and 800 °C, respectively. In Fig 16a, the strain-time evolutions of the two devices are shown with (a) temperature and (b) stress also plotted in dashed lines using the second y-axis. For pedagogical reasons, the strain is given in mm instead of the usual [-] or [%]. There are three segments of the routine: heating to the lower (start) temperature (1), pre-cycling in zero load control (2) and load by thermal cycling in a locked state (3).

As can be seen in steps (1) and (2), the two devices show exactly the same strain when the load is zero. Then, as the specimen is locked and loading by thermal cycling starts (3), the extensometers register strains of about -0.1 mm (contact extensometer) and -0.3 mm (laser extensometer) at the end of the first compression. It can be commented that $L_0=12$ mm for both devices, fixed for the contact extensometer and manually set for the laser extensometer. Thus, the results show that there is an actual difference in measured strain, a difference which grows with the number of cycles.

So, which device shows the correct strain? A way of estimating is to look at the thermal strain during pre-cycling at zero load (2), which is basically a dilatometry test between the lower and upper temperature limits. This shows the strain contribution originating purely from thermal expansion. During thermal cycling in a locked state, this thermal strain, along with a

small elastic strain, is transformed into plastic strain. Thus, the measured strain is not expected to be much higher than the thermal strain during pre-cycling. Since it is slightly higher in the case of the contact extensometer, and *several times* higher in the case of the laser extensometer, the laser extensometer appears to show unreasonably high strain.

One reason for this potentially large error is that the laser extensometer cannot keep track of the speckle patterns during deformation. The speckle pattern depends on the scattering angle of the diffracted laser light which depends on surface topology, for example including the orientation of surface-exposed grains. With this in mind, the tracked speckle patterns in the green boxes are probably changed because of strain itself (leading to a changed diffraction). The strained grains give a change in speckle pattern making it move which is then misinterpreted as a strain. (This idea was suggested by Joakim Lindblom, see acknowledgements). However, since the two devices show the same character of the strain curve, they can both be used to investigate tendencies in strain. For the present study, this means that the strains presented in appendix 1 are most likely too high but, nevertheless, show the correct behaviour.

It can be commented that a similar measurement was made for SiMo51 which showed the same result.

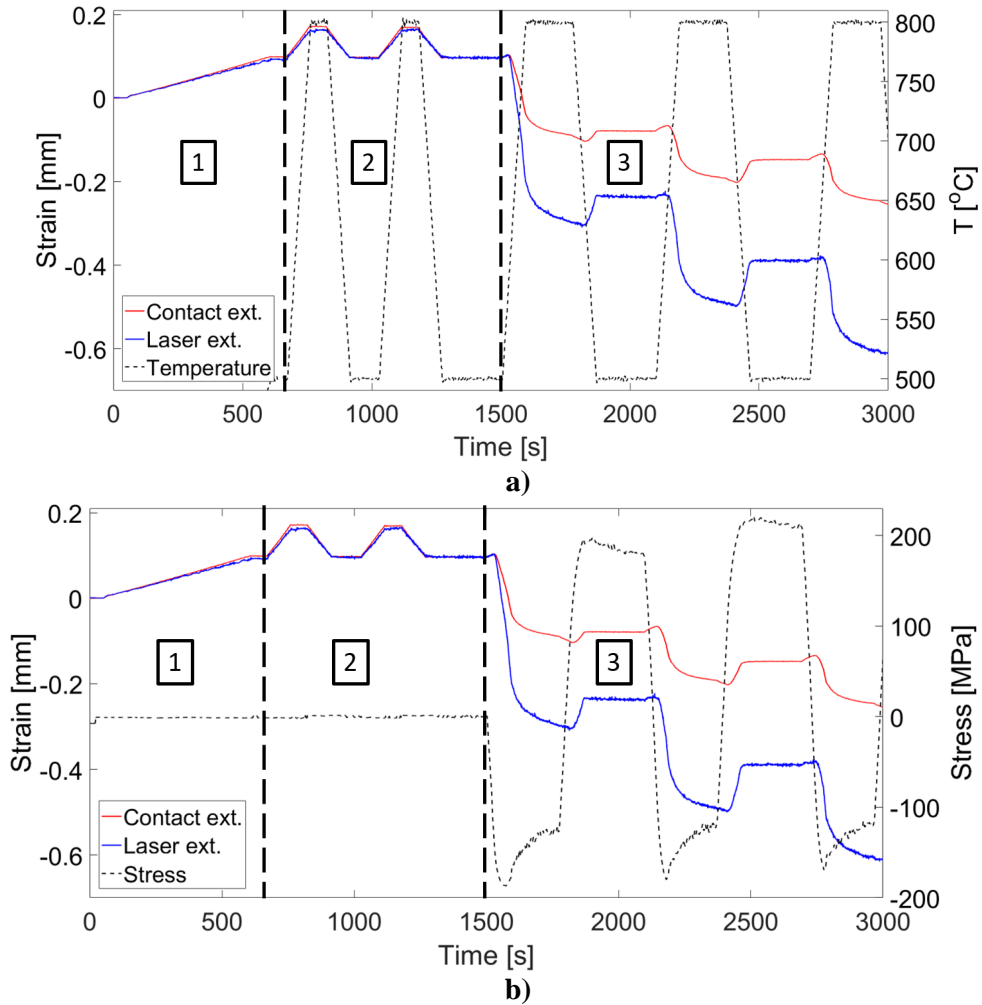


Fig 16. Strains registered during thermal cycling (SRTC) of HK30 using the contact and laser extensometers. Temperature (a) and stress (b) were also plotted using the second (right) y-axes. (1) Heating to the lower (start) temperature. (2) Pre-cycling at zero load, (3) Load by thermal cycling in a locked state.

4.3. Sequential tensile test (STT)

STT was carried out at Volkswagen, Wolfsburg, Germany. A Zwick/Roell Kappa 050DS test rig was used, see Fig 17. The machine allows testing up to 1400 °C using a radiation furnace. Six thermocouples (the middle used for control) were tied to the specimen. The temperature gradient was about ± 2 °C over the measuring length. Strains were measured using two ceramic contact extensometers (see Fig 17b) which were fastened to the knife edges of the specimens.

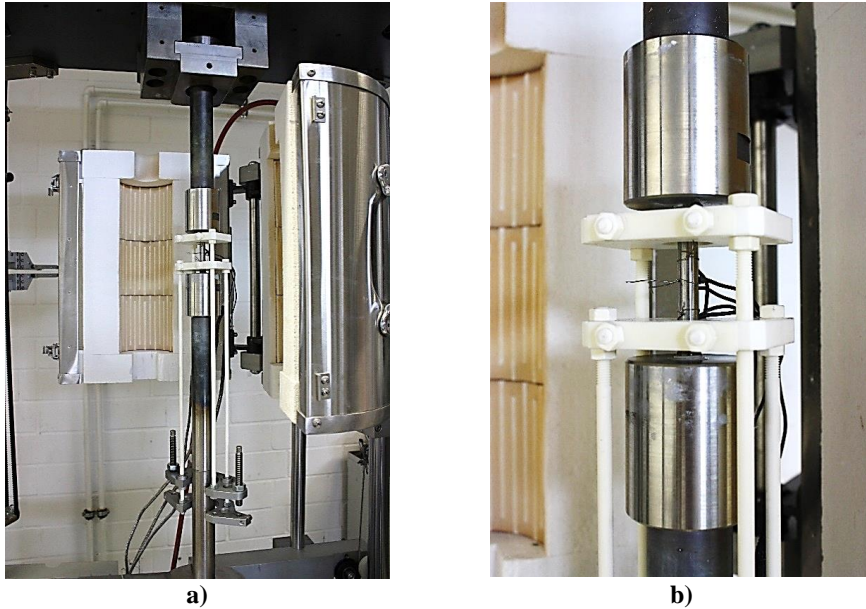
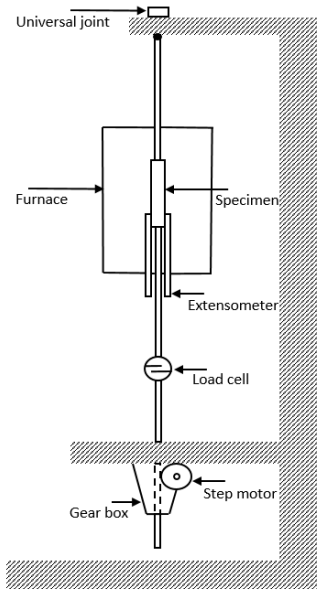


Fig 17. a) Zwick/Roell Kappa test rig used “Sequential tensile tests”. b) Ceramic extensometers setup.

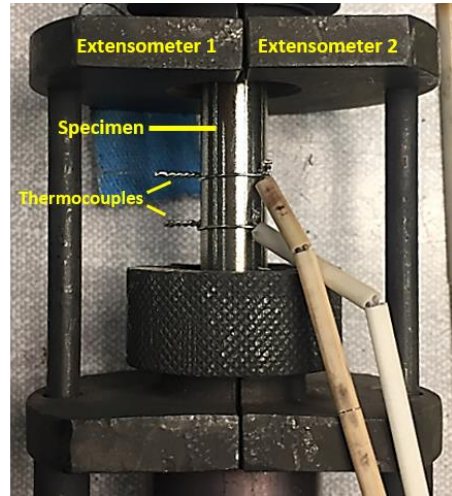
4.4. Constant-load (CL) creep test

These tests were carried out at the research institute of Swerim, located in Kista, Sweden. Tests were conducted following the international creep standard SS-EN ISO 204:2018 [38]. Instead of the traditional way of applying the load through dead weights, a step motor was used. The step motor loads the load cell and specimen and uses the feedback signal from the load cell to control the load to a constant value, obtaining ± 3 N from the set-point (well within the requirement of 1 % of the load). Strain was measured with two contact extensometers which were fastened to the knife edges of a specimen, obtaining an accuracy of ± 100 nm. Three thermocouples were tied to the gauge length, with the middle one used for control. A temperature gradient of ± 1 °C was obtained which is also well within the requirement of ± 4 °C between the set and obtained temperature.

An illustration of the setup of the creep test rig is shown in Fig 18a and an image of the specimen, the two extensometers and two of the thermocouples (a third upper one is missing in the image) is shown in Fig 18b.



a)



b)

Fig 18. Setup of constant-load creep tests. a) Schematics of the rig, b) Specimen, extensometers and two thermocouples (a third is yet to be tied above these two).

4.5. Regular, “non-sequential”, tensile tests

Some regular, non-sequential tensile tests were carried out, see appendix 3. In those tests, an MTS-810 servo-hydraulic test rig, with axial loading capacity of 100 kN, was used. The rig is equipped with an induction heating system identical to the one used in the test rig for SRTC. The temperature gradient is about ± 10 °C over the measuring length (as told by an operator of the machine). A similar contact extensometer, attached with aluminium oxide pins ($L_0=12$ mm), was used for measuring the strain. The test rig is located at Scania CV AB, Södertälje, Sweden.

4.6. Oxidation tests

In the third study, see appendix 3, oxidation testing was also conducted in air at 700 °C using a Carbolite CST 12/70 furnace. The furnace, originally intended for a tensile test rig, was flipped and placed horizontally on a desk. It was opened through hinges and specimens were placed directly on the inner ceramic lining. The area where the specimens were placed was checked by manually measuring the temperature using a thermocouple (type K). In this area, there were deviations of ± 5 °C from the set temperature (700 °C).

4.7 EBSD

In all EBSD-measurements, specimens were polished using oxide particles (Buehler Colloidal Silica polishing suspension). A LEO 1530 FEG-SEM, with the EBSD detector “Symmetry”, was used. Various step lengths were used depending on the accuracy needed.

For post-processing of data, the software analysis platform Aztek was used together with the “Tango” software, included in the “Channel 5” package. Local misorientations were calculated in each pixel as the average of the misorientations to the eight surrounding pixels.

5. Results and discussion

5.1. Mechanical response to thermal cycling

In the first study (see appendix 1), thermally induced, cyclic deformation was studied through SRTC (stress relaxations with thermal cycling). The study included SiMo51 and SiMo1000.

The method, described in previous sections, is similar to TMF-OP (out of phase) but differs regarding the control parameter. By standard [4], TMF-OP is carried out using strain control while SRTC is instead controlled by specimen length. More precisely, in TMF-OP the strain signal, measured by an extensometer attached to the specimen gauge section and calibrated for a specified measurement length, is used to control the movement of one of the specimen grips, producing distinct ramps in strain (strain amplitudes). In SRTC, the positions of both grips are instead kept constant, meaning that the specimen is locked in its full length. The idea is that even if the total specimen length is constant, local strains can be registered by the extensometer within the measurement length. Thus, by having a high temperature and high stress along the gauge, it is possible to provoke and measure local plastic deformation, still keeping the full specimen length constant. Due to the condition of constant specimen length, such a deformation, for instance a heavy compression right in the middle of the gauge section appearing during heating, must be balanced by elastic specimen extension in surrounding, slightly colder areas of the gauge section, working as loading springs. This deformation produces a thicker mid-section which during cooling, and corresponding reversion of stress into tension, resists plastic deformation better than the surroundings. Hence, new local deformations in tension may occur in the specimen gauge section but slightly (or partly) outside the measurement length. This process may be repeated every cycle, changing the specimen geometry considerably. Indeed, this was directly observed: in some cases, the middle part of the gauge was very thick while areas a bit further away were considerable thinner compared with the original diameter.

A possible advantage of using this procedure compared to TMF-OP is possibly that the condition of a locked specimen length and spontaneous strain evolution is more realistic with regard to the real conditions of exhaust manifolds (compared to strain control). It is also beneficial that the method gives valuable output without strain-control, which is sometimes difficult to achieve. Even with the most reliable extensometers, the PID-parameters of the system need to be trimmed in, which is not trivial.

Most importantly, the study in appendix 1 led to an understanding of the mechanical response during thermal cycling and also showed the effect of changing the various parameters. The illustration from appendix 1 is shown below in Fig 19 and is representative of the behaviour of both SiMo51 and SiMo1000. Hypothetical yield stress curves were added as grey, dashed lines and the segments of the loop were coloured in blue or red for elastic and plastic events, respectively.

The specimen is locked at (1), and as it is heated a compressive stress develops (1-2), see Fig 19a. Looking at the corresponding elastic strain change, b), it is practically zero. At (2), the

yield stress is exceeded followed by a stress relaxation (2-3), see a), and heavy compressive straining, see b). In reality, deformation hardening was small and is exaggerated in (2-3). (3-4) mark the high temperature hold which was introduced to allow further creep deformation during constant temperature. For later investigations, the second paper, appendix 2, this was the most important segment. During (4-5), the load is reversed by cooling of the specimen. At (5), the yield stress is exceeded on the tensile side, giving rise to a strain increase in b). Then, as the yield stress becomes higher at lower temperatures, another segment of elastic deformation (6-7) is followed through. (7-8) is the low temperature hold which, if this lower temperature is high enough, allows strain increase due to creep deformation, see b). In (8-9), the load is again reversed by heating. Since the stress is insufficient to cause yielding, (8-9) only gives small elastic straining, see b). Due to the curvature of the hypothetical yield curve, plastic deformation occurs again but only temporarily at 9-10, leading to substantial increase in strain. Elastic deformation (10-11) proceeds until the yield stress is reached, creating a new compression. Since the cycles did not overlap, the specimen “climbed” towards positive (as illustrated) or negative strains. Climb towards negative strains was more common and resulted in “barrelling” which could be readily observed after many cycles.

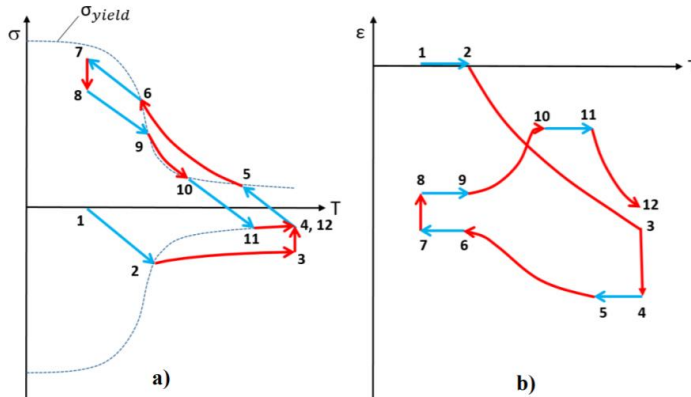


Fig 19. Illustration of SRTC (1.5 thermal cycles) with stress a) and strain b).

Blue = elastic segments, Red = plastic segments.

5.2. Comparing stress relaxations with thermal cycling (SRTC), sequential tensile tests (STT) and constant-load (CL) creep tests

In the second study (see appendix 2), the method SRTC was dedicated to the purpose of obtaining creep data which was compared with results of STT and CL. All four materials were tested: SiMo51, SiMo1000, D5S and HK30. SiMo51 was tested by all three methods while the other three were only tested by SRTC and STT. SRTC and STT are generally quick methods, or at least they are intended as such, while the CLs are costly and associated with longer times. Obviously, the time to acquire data depends on settings of stress and temperature; for instance, temperature interval and heating/cooling rates (SRTC), selected strain rates (STT) and set load (CL).

In Fig 20, a comparison of SRTC and STT results from testing of HK30 is shown in a Norton plot. The SRTC test was conducted at 300-800 °C but only the stress relaxation and strain

rate evolutions during the high temperature holds (800 °C) of cycles 1-91 have been included in the plot. For STT, data at 800 °C, including obtained strain rates and saturation stresses, are included with the associated regression line. As can be seen, the data sets agree almost perfectly. From this and similar plots including the other materials, it was concluded that creep in tension, by tensile testing, and compression, by stress relaxations, are the same for these materials. It can also be noticed that creep rates remain unchanged with the number of cycles. This is valuable to know in various fatigue lifetime simulations which need input of cyclic creep parameters, which in this particular case are the same as the monotonic ones. For instance, the effect of adding creep models to fatigue lifetime simulations of exhaust manifolds have been studied by Seifert et al. [39], [40].

The same tendencies, with small modifications, could be seen for the other three materials SiMo51, SiMo1000 and D5S. See more details in appendix 2.

Comparing all three methods, applied to SiMo51 at the upper limit test temperature of 700 °C, things became more complicated. In the case of SRTC, an extra-long hold time of 8.3 h was introduced to really enter the creep regime in compression. Just as for other comparisons, only the high temperature (700 °C) hold time data was evaluated. As can be seen in Fig 21, the SRTC and STT results agree almost perfectly at higher stresses, just as for HK30 in Fig 20. At lower stresses, where the results of the CLs can be found, the strain rate evolution of the SRTC test abruptly goes down to practically zero, just as if there was a critical stress for creep deformation. The CLs fall about one decade lower in strain rate compared with STT and SRTC (found at higher stresses), but the data sets have about the same slope, indicating a similar creep mechanism. The cause of the shift of one decade in strain rate could not be fully verified. However, in appendix 2, oxidation is briefly discussed as a possible reason. The thought behind this is that the growing oxides increase the specimen diameter during primary creep and thus lower the stresses/minimum creep rates in relation to those of SRTC and STT (where times for oxidation were much shorter). Quite naturally, the credibility of this theory depends on the load-carrying ability of the oxide scale as a whole, which is not established. To avoid confusion, it can be commented that in estimations of the effect of oxidation on creep strain rates (appendix 3) the load-carrying ability was instead set to zero by assuming that the inwards-growing oxide layer did not carry load. See paragraph 5.3, or most detailed, appendix 3. Another reason could be that different casting batches were used for SiMo51 in the CL tests (one batch) compared with STT/SRTC (another batch), which could give rise to differences in microstructure (even if such could not be observed). The chemical compositions of the batches were generally very similar, but one difference was that the batch used for the CL test of SiMo51 contained 0.20 wt% Ni whereas that used for STT/SRTC contained 0.03 wt% Ni which could give a difference in solution strengthening.

The critical stress for creep deformation, as mentioned above, was only observed in the SRTC test. A possible explanation can be traced to the level of pre-deformation associated with each test. To begin with, the SRTC stress relaxation included in Fig 21 was preceded by deformation (compression) of 2.1 % during the heating ramp prior to the hold time. In addition, 1.2 % strain accumulated during the actual hold time. With the STT tests, the present settings (see Table 2) always result in a pre-deformation of 2 % strain (by tensile stress). In the CL test of 14 MPa, on the other hand, pre-deformation was only 0.4 % at the point of reaching the minimum creep rate. Thus, pre-deformations were much larger for the two faster methods compared with the slow CL test. This could explain the creep stop, i.e.

why the strain rates of the SRTC test go down to zero at about 14 MPa whereas the CL test of 14 MPa still gives a measurable minimum creep rate of about 10^{-9} s^{-1} , see Fig 21.

Regarding prolonged “steady state” or a direct transition to tertiary creep, the compressive SRTC sequences probably only allow steady state since cracks generally do not grow in compression. However, a comparison is meaningful in the case of STTs and CLs. The STT tests, due to the large pre-deformation (2 %), probably exhibit a steady state rather quickly. This is confirmed by the plateau of the first sequence (10^{-4} s^{-1}) of the 700 °C STT test of SiMo51, previously shown in Fig 11. Additionally, the following sequences in Fig 11 also show plateaus (except the second), indicating steady state. The CLs, on the other hand, quickly go into tertiary creep (although the curves level out before, see paragraph 5.3). An explanation of this difference is the aspect of time: in a creep test, damage is allowed to grow more slowly and cause a direct transition. In the tensile tests, dislocations are instead quickly pumped into the material and a steady state is reached just as fast – but there is not enough time for damage to grow.

Another viable cause for a quick transition is oxidation, see paragraph 5.3.

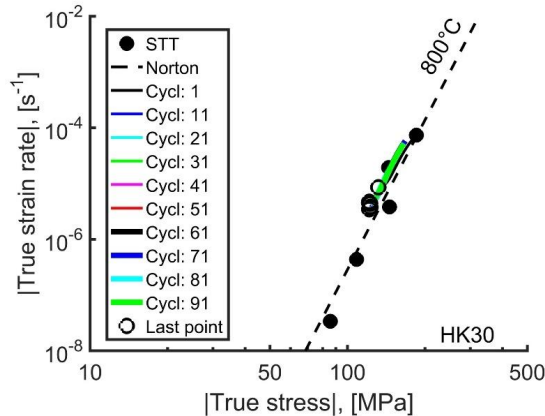


Fig 20. HK30, cycled between 300-800 °C. Results at 800 °C, including the stress-strain rate evolution of the hold time (SRTC) and strain rates-saturation stresses (STT).

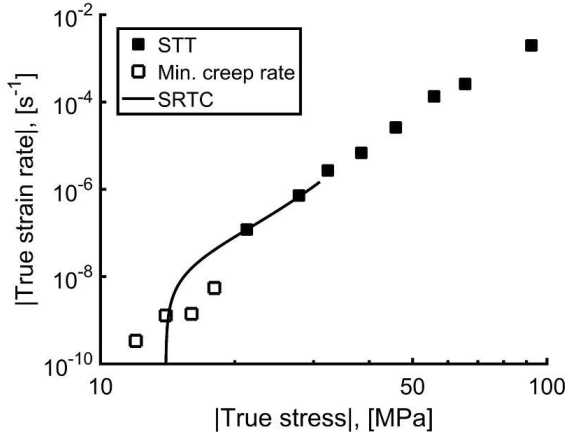


Fig 21. Norton plot of SiMo51 including STT, CL and SRTC (hold time of 8.3 hours in compression) at 700 °C.

The comparison between CL and STT could also be briefly commented for the materials HK30 and D5S, which were both tested at 750 °C in STT and CL.

For HK30, STT at 750 °C was not included in appendix 2, since the deformation hardening observed in the STTs at 750 °C was too heavy and no “plateau”, i.e. saturation stress, was reached in any of the sequences. Thus, no sound comparison could be made with the CL tests at 750 °C in that case. A suggestion for future work could be to test HK30 by avoiding high deformation rates (e.g. 10^{-4} - 10^{-3} s $^{-1}$).

In the case of D5S, the CL data at 750 °C was not shifted to a lower level compared to the STT data at 750 °C, but in that case the slopes of the two Norton plots (the n -values) differed instead. In summary, there is no consistency in the difference in results between the STT and CL for the materials. Hence, the discrepancies could simply be related to differences in microstructure and chemical composition between the various casting batches which were used for each test.

5.3. Creep of SiMo51 at 700 °C, focusing on “Two-stage” tertiary creep

In the third paper, see appendix 3, the same CL specimens as in appendix 2 were investigated regarding the microstructural damage resulting from the creep tests. Additionally, this damage was compared to that of regular tensile tests and also to oxidation tests. All tests were carried out at 700 °C since that was the temperature of the CL tests.

The true strain rate curves of the four CL tests are shown in Fig. 22 with strain rate as a function of strain (log-log). As can be seen, primary creep regimes are followed by tertiary creep. However, by plotting the very early parts of the creep curves (primary creep) with a linear time scale instead of a logarithmic strain scale, see Fig. 23, it can also be observed that the curves more or less “level out” before entering tertiary creep, indicating that they for a short while were in, or close to, a steady state. Fig. 23 is a close-up of Fig. 8 in appendix 3

and the additional points (black squares) were in that case used to evaluate the true strain rate-time dependence.

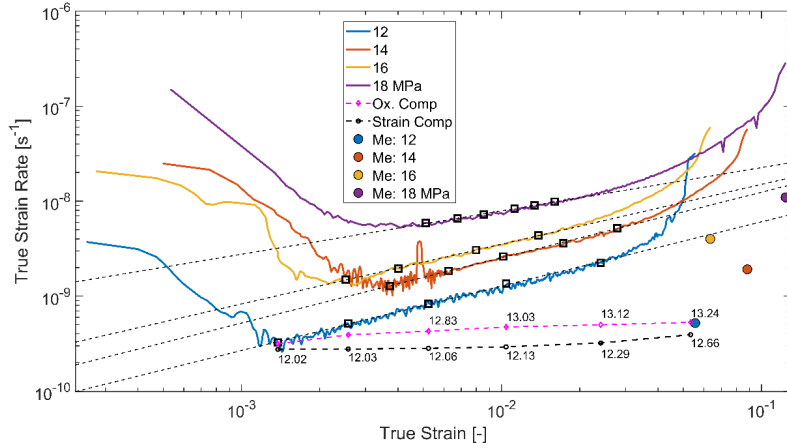


Fig. 22. True strain rate (creep rate) as a function of true strain. SiMo51, tested at 700 °C. Numbers beside points indicate two hypothetical stress evolutions of the 12 MPa sample taking area reduction into consideration with respect to volume conservation (Strain Comp) and with respect to surface oxidation (Ox. Comp), respectively. (From appendix 3).

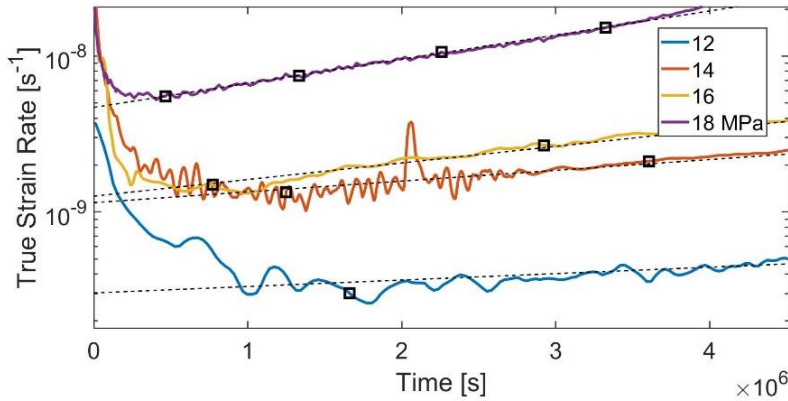


Fig. 23. The first part of the constant-load creep tests of SiMo51 with a linear time scale.

Referring to Fig. 22 again, primary creep was followed by a “first” tertiary creep stage which is seen as a linear segment in the log-log plot of true strain rate as a function of strain. This is in turn followed by a “second” tertiary stage, being more accelerated in nature. A question being raised was how the tertiary stage could be subdivided into two stages, i.e. what caused the first stage. Three possible reasons were considered: i) reduced load-carrying area due to pure straining (volume conservation), ii) reduced load-carrying area due to oxidation and iii) softening from creep damage. In calculations of the various contributions (Fig. 22), the 12 MPa specimen served as an example.

The contribution from pure straining, i), was obtained by calculating the true stresses at certain true strains, using the technological stress of 12 MPa and the constant-volume approach. The stress was then inserted into Norton's creep law (obtained by regression analyses of the minimum creep rates) to obtain a "strain-compensated" strain rate. See the black line, labelled "Strain Comp", in Fig. 22. As can be seen, the effect of pure straining on stress and resulting creep strain rate is rudimental during the "first" tertiary stage. Therefore, it cannot be held responsible for the measured increase in strain rate.

Secondly, the effect of oxidation, ii), was estimated by plotting the oxide thickness obtained from one (separate) oxidation test and the four creep tests. For more details, see appendix 3. In Fig. 22, each strain corresponds to a time which, from the oxidation curve, was translated into an oxide thickness. Since about half of the oxide grew inwards and decreased the metallic area, the total oxide thickness, plotted in the oxidation thickness curve, was divided by 2 and removed from the original specimen radius. The remaining area was finally translated into "oxidation-compensated" stresses which, by Norton's law, in turn were translated into strain rates, see "Ox. Comp" in Fig. 22. As a last check, the purely metallic area of each fractured specimen was measured with the light optical microscope. These areas were translated to stresses (since the load is constant) and strain rates (again through Norton's law) and are indicated by filled, coloured circles. As can be seen, the oxidation compensated strain rate is not high enough to account for the measured rate. Neither is the strain rate calculated from the purely metallic area. It is also interesting to note that in the "first" tertiary stage, the last strain rate of "Ox. Comp" (marked 13.24) agrees perfectly with the strain rate calculated from the purely (measured) metallic area (filled blue circle). This confirms that practically all area reduction was from oxidation and that the original radius was correctly reduced by only half of the total oxide thickness.

Rejecting the options listed above, the increasing strain rate in the "first" tertiary stage was attributed to accumulating creep damage, iii). The existence of such creep damage was confirmed through microscopical investigations. In Fig 24, the various types of creep damage are indicated, this time with the 14 MPa specimen serving as an example. (1) is a typical form of creep cavitation, located at grain boundary carbides. (2) is cavitation around the graphite nodules. In quick tensile testing, such damage also occurred but in the shape of large ovals around the nodules. In the creep tests, such ovals are clear signs of locally elevated deformation rates. (3) is the linkage of ovals/cavities/nodules into larger cracks. When connected to air, this type of "dimple" crack is oxidized, see (4). (5) indicates the outer oxide scale.

Connecting this to the discussion on the "two-stage" tertiary creep, (1-2) are related to the first stage and (3) to the second stage of tertiary creep.

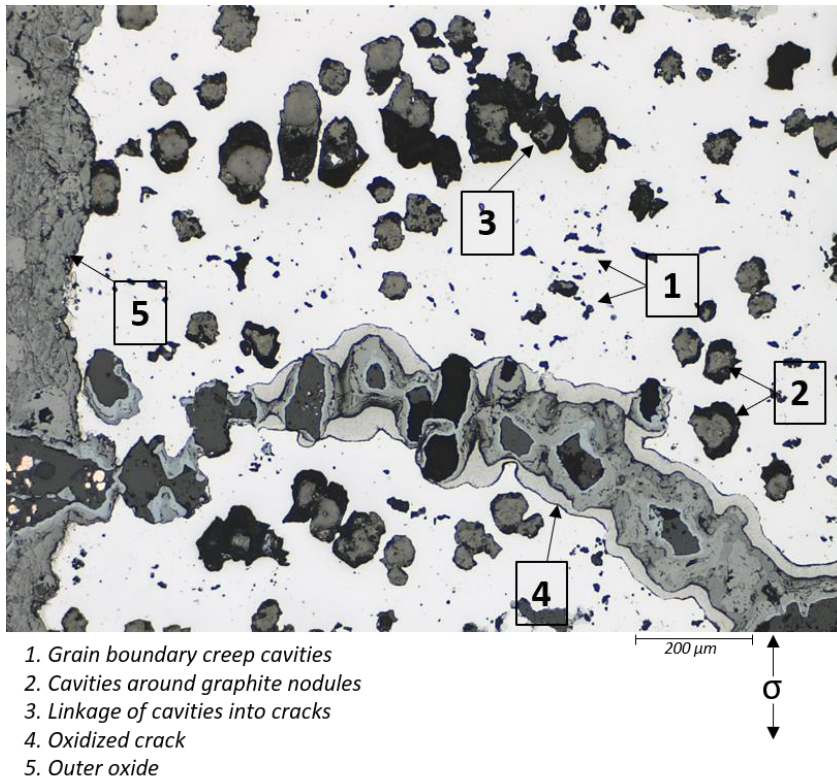


Fig 24. Various types of damage in SiMo51, CL tested by 14 MPa at 700 °C ($t_r = 114$ days).

5.4. Creep behaviour and damage of HK30 at 750 °C

In the fourth paper, the austenitic cast steel HK30 was creep tested at 750 °C, applying loads corresponding to initial stresses of 50, 53, 59, 70 and 95 MPa. The higher temperature of 750 °C, compared to 700 °C for SiMo51, was selected as HK30 is regularly used for more demanding applications, e.g. manifolds in gasoline engines. Compared with SiMo51, this austenitic steel showed a more conventional creep behaviour. At higher stresses, there were direct transitions between primary and tertiary creep whereas at lower stresses, more prolonged secondary creep was accomplished, see Fig 25.

It can be commented that the creep curve of the 70 MPa specimen initially exhibited an unexpectedly low creep rate relative to the others which, however, instantly increased to a new level. Since the new level agreed better with the evolution of the rest of the creep curve and also with the rates of the other tests (by the Norton plot), it was selected as the “real” minimum creep rate. It can be noted that without this adjustment, the data would not follow Norton’s law. The phenomenon was possibly attributed to a sudden activation of creep in one of the large grains by a chain-reaction with another grain (a redistribution of the stress). See appendix 4 for more details.

In addition to the conventional creep curves, conventional creep cavitation was observed, especially in the most long-lasting specimens tested at 50 MPa and 53 MPa. Since

documentation of the 53 MPa specimen was not included in the paper, appendix 4, it is added here instead. As can be seen in Fig. 26, showing unetched material, creep cavitation grows as isolated segments which, in other spots, see b), have connected into larger cracks.

Other effects during creep were surface re-crystallization and particle precipitation. Both are featured in Fig. 27. In Fig. 27a, an orientation map of a cross-section including a grain-boundary creep-crack along with the re-crystallized specimen surface (bottom) is shown. As can be seen, the crack is located at a grain boundary of the original, un-recrystallized material whereas only a hint of a crack can be observed in the recrystallized layer. This indicates an effective grain boundary sliding mechanism in the recrystallized layer, preventing the crack from entering this region. Furthermore, much smaller recrystallized grains can be found near the crack which is indicative of a dynamic recrystallization process.

Regarding the creep testing artefact from recrystallization, it was considered to not fundamentally influence creep as the layer was too thin. Altogether, it seems as though the recrystallized layer was like a ductile skin of the material, but without adding any apparent strength. The original material cracked along the original grain boundaries, seemingly with no relation to the recrystallized layer. As a result, the crack may be difficult to see on the specimen surface, although being very clear inside the material.

In the original, untested HK30 material, only $M_{23}C_6$ precipitations could be found. During creep exposure, two new phases precipitated: sigma phase and, likely, G phase. The distribution of the three phases is shown in Fig. 27b, a highlighted area of Fig. 27a. As can be seen, the sigma phase was bulkier compared with the others and was preferentially located at original, un-recrystallized grain boundaries and also recrystallized grain boundaries. The cracks do not grow through the precipitations but around them, as evidenced by Fig. 27b. Thus, the particle-matrix interface appears to be the weak link of HK30.

As previously shown, Fig 6, HK30 has a very big grain size of several mm (up to cm size). From a creep perspective, this may be an advantage as the grain boundary area is relatively small. However, only a very few, large grains allow less rotation as a response to deformation, generally leading to increased brittleness.

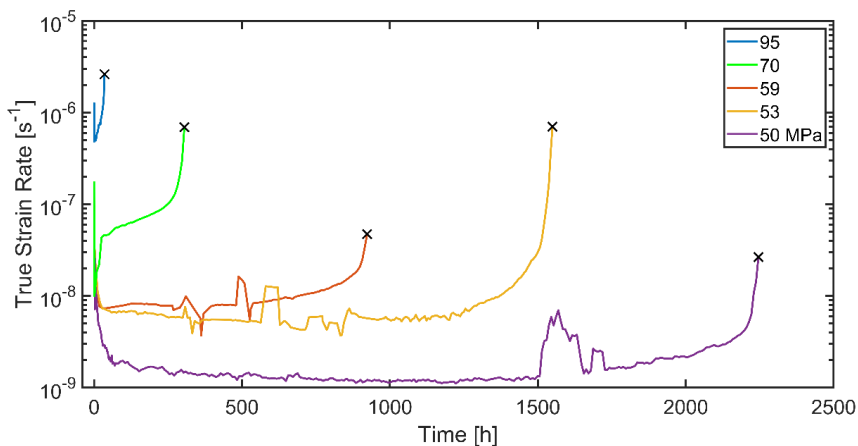


Fig 25. HK30, creep tested at 750 °C. Creep strain rate as a function of time (semi-log axes).

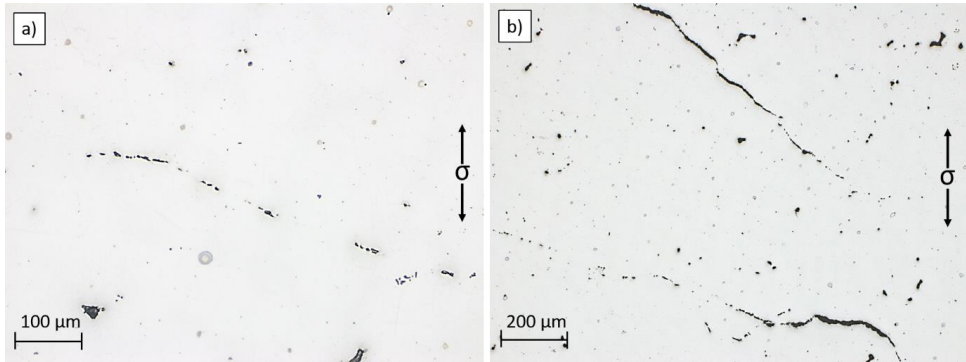


Fig. 26. a), b) Creep cavitation/cracks in HK30 specimen tested at 53 MPa and 750 °C, $t_r=1,557$ h.

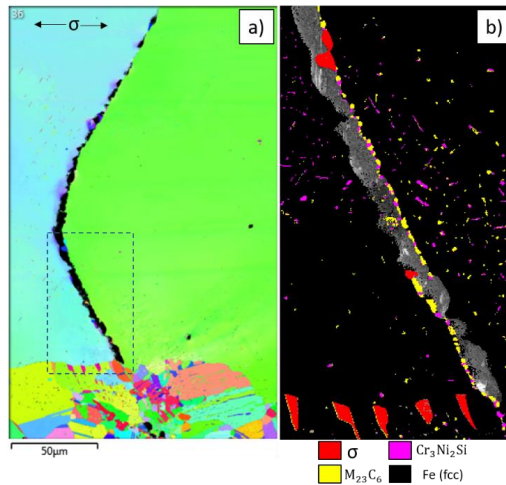


Fig. 27. a) Orientation map featuring a grain boundary crack and the recrystallized surface layer (bottom), b) phase precipitations in the recrystallized layer and along the crack. The specimen surface is just below the bottom in the images.

5.5. Creep behaviour and damage of D5S at 750 °C

Since it is used for similar conditions as HK30, D5S was also creep tested at 750 °C. The creep strain rate curves are shown in Fig 28. This material shows the same trend as HK30 with quick transitions between primary and tertiary creep at higher stresses and more or less pronounced secondary creep at lower stresses.

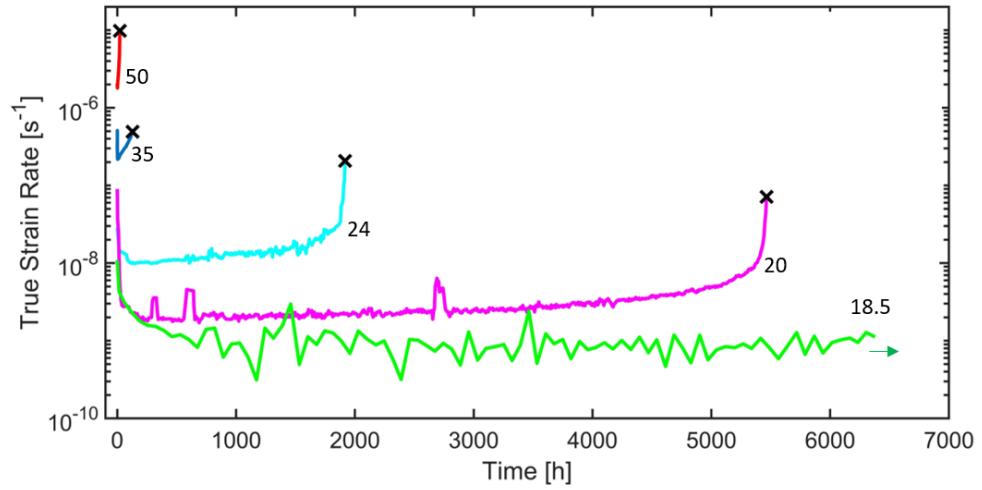


Fig 28. D5S, creep tested at 750°C. Creep strain rate as a function of time (semi-log axes).

In order to see the damage originating purely from secondary creep, the 18.5 MPa specimen was interrupted after 6494 h. For this specimen, and for the shorter lasting specimen of 20 MPa, the documented cavitation and damage is shown in Fig 29. As can be seen, small cavities have emerged around graphite nodules in both materials. Since 20 MPa was tested to rupture, it also contains clear traces of tertiary creep in the form of shear cracks (see Fig 29d).

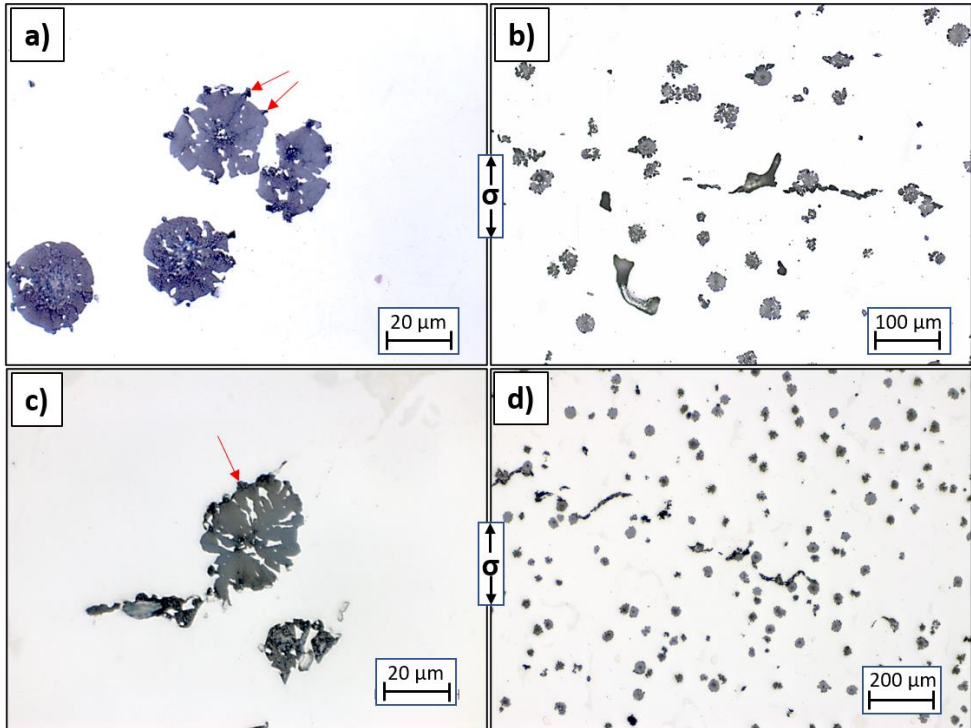


Fig 29. Microstructure of creep specimens of D5S tested at 750 °C. a) Creep cavitation (18.5 MPa), b) same as a) in lower mag. c) creep cavitation (20 MPa), d) shear cracks (20 MPa).

The 20 MPa specimen was also investigated using EDX/EBSD and it was revealed that significant amounts of Cr_7C_3 carbides along with larger particles, including $\text{Fe}_2\text{Ni}_2\text{Si}$ and an unidentified carbide, had precipitated during creep exposure. The effect on creep rate is hard to account for as there are at least two opposing mechanisms: decreased solution strengthening and increased precipitation hardening (depending on the particles). Cr_7C_3 carbides precipitated both in the shape of plates and small spheres while the other particles were large and irregularly shaped. Images of the various precipitations and their corresponding EDX maps can be found in appendix 5.

In local misorientation measurements, sub-grain boundaries of about 1° , i.e. very small misorientations from deformation, were measured. The corresponding misorientation images (maps) show the local imbalance in dislocation density and thus only indicate the degree of plastic deformation. It could be emphasized that gliding dislocations produce plastic deformation whereas locally stored dislocations, with an imbalance in the sum of Burgers vector produce a local misorientation, which is being observed. At higher temperatures recovery and annihilation often restores the lattice leaving no apparent trace of the strain created by gliding dislocations while shaping more well-defined cell walls and sub-grains with clearer orientation differences. Thus, the local misorientation technique is useful to show tendencies in the dislocation microstructure being formed, rather than measuring local deformations. Compared with a regular misorientation measurement, which gives the orientation from one pixel to the next, the local misorientation in each pixel is the average of

the misorientations between this pixel and the surrounding pixels (3*3 matrix). This noise-reducing moving average filter is sometimes critical for observing the very small strains/misorientations due to creep.

Local misorientations were measured on untested and creep tested (20 MPa) materials, see Fig 30. In Fig 30a, it can be seen that even the untested material contains low angle misorientations/subgrain boundaries of about 1° . In Fig 30b, the effect of creep deformation is seen as a significant increase in subgrain boundaries of around 1° .

In addition, the same areas are shown as “regular” orientation maps in Fig. 31. There, it can be noted that both untested and creep tested materials contain additional subgrain boundaries ($>2^\circ$) but there is no apparent increase. Hence, creep adds a lot of 1° subgrain boundaries to the material, in accordance with Kassner et al. [19].

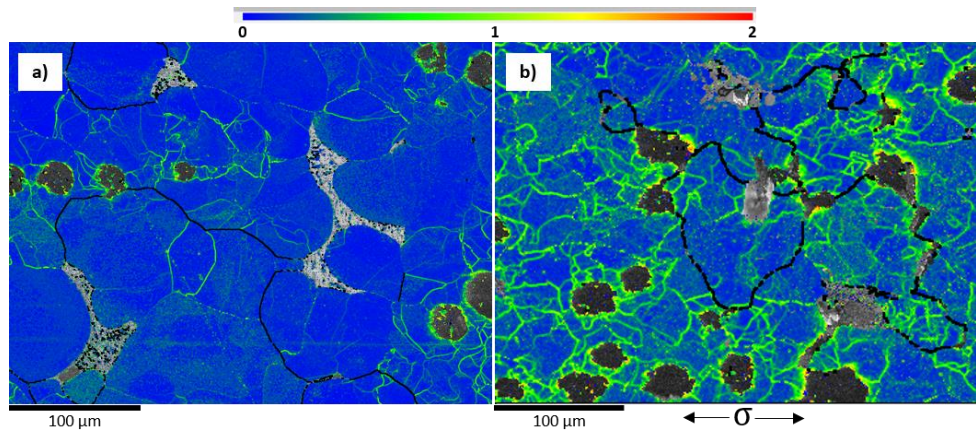


Fig 30. Local misorientation ($0-2^\circ$) in D5S, a) untested and b) creep tested (20 MPa) materials.

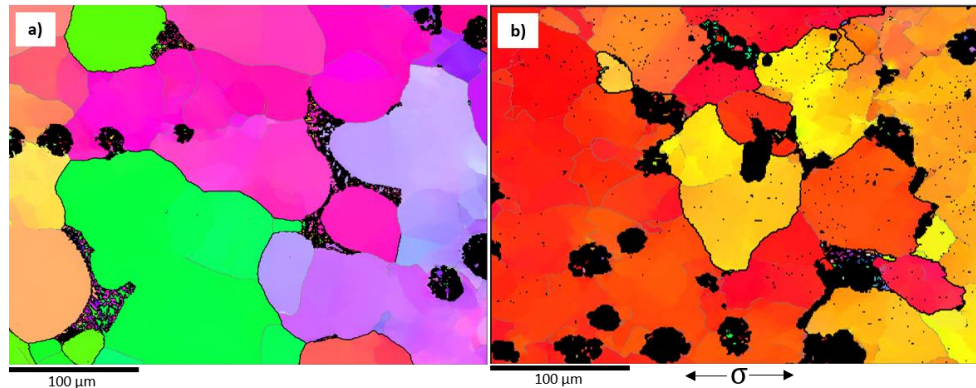


Fig. 31. “Regular” orientation maps of the areas in Fig 30 with a) untested and b) creep tested (20 MPa) materials. High angle grain boundaries ($>15^\circ$) are shown as thick black lines while low-angle boundaries ($>2^\circ$) are shown as subtle gray lines. Red = {001}, Green = {101}, Blue = {111}. Reference: Y-axis (in the specimen plane).

6. Summary

Four cast materials, including three ductile cast irons and one cast steel, were tested mainly with regard to slow and fast plasticity. The first two papers (see appendices 1 and 2) treat the method development and data output analyses associated with the three methods SRTC, STT and CL. The third, fourth and fifth papers are more focused on damage, mainly from creep but, in the third paper, also from oxidation and tensile testing.

The first paper (appendix 1) mainly describes the mechanical response to thermal cycling and the method of SRTC as an alternative to the more traditional TMF testing. In general, SRTC is easier to conduct as it is not strain-controlled. The thermal cycling loops were described in terms of elastic and plastic deformation segments. It was shown that they carry essential information about mechanical properties, such as evolution in flow stress over the selected temperature interval. Several test parameters, such as temperature interval, heating/cooling rates and hold times were changed to see the various effects. The contributions in strain during each part of the thermal cycle were compared.

In the second paper (appendix 2), the hold-time stress-relaxation-data, generated from thermal cycling using SRTC, was compared with sequential tensile tests and constant-load creep tests. The results were inserted into “Norton plots”, double logarithmic stress-strain rate diagrams which are regularly used to compare creep data. Results obtained by the two fast methods, SRTC and STT, in many cases showed perfect agreement. Since SRTC results were often evaluated with regard to hold time compression at the upper temperature of thermal cycling while STT includes tensile loading, the results showed that creep rates are independent of load direction. “Cyclic” creep rates were more or less unchanged with the number of cycles. At 700 °C, the CL data set ended up one order of magnitude lower (in strain rate) compared with SRTC and STT but had the same slope which indicates one common creep mechanism.

In the third paper (appendix 3), the damage from the CL tests of SiMo51 (appendix 2) was investigated. Tensile tests and oxidation tests were also carried out for comparison. As described above, primary creep was more or less directly followed by a “two-stage” tertiary creep. Out of these two stages, the first accounted for the largest part of the creep life and was therefore of biggest interest. After considering pure straining and oxidation, rejecting both, it was attributed to cavitation around graphite nodules and at the grain boundaries. The second tertiary stage was attributed to the usual characteristics of tertiary creep, namely coalescence of smaller creep cracks into larger ones. Tensile test damage was associated with necking and large oval voids around the graphite nodules.

In the fourth paper (appendix 4) the cast steel HK30 was investigated in constant-load creep testing at 750 °C. During creep, sigma phase and presumed G-phase precipitated. The phase identities were verified using EBSD and Thermo-Calc. As a specimen preparation artefact, the surface of the specimens recrystallized during creep testing. However, since the recrystallized zone was so thin and apparently did not crack, it is not considered to have had any real effect. Instead, cracks propagated in grain boundaries, predominantly following grain boundary particle interfaces of the original, “un-recrystallized” material. Ultimately, the large grains, sometimes exceeding the specimen diameter, were considered the big weakness of HK30.

In the fifth paper (appendix 5), D5S was CL tested, also at 750 °C due to similar service conditions as HK30. The creep damage reminded of the one observed for SiMo51: “delicate” cavitation around graphite nodules at low stresses and long times, and large oval voids around nodules at high stresses and short times. For both SiMo51 and D5S, the delicate cavities were considered a time-dependent creep-phenomenon, likely following one of the many theories on creep cavitation. The large ovals were attributed to strain-dependent dislocation glide. Cr₇C₃ particles precipitated together with larger particles, including Fe₂Ni₂Si and an unidentified carbide. The effect from the observed precipitation is complicated to predict as there is both decreased solution strengthening and increased precipitation hardening. Creep deformation created a lot of additional subgrain boundaries of about 1° in the material.

7. Conclusions

In the present study, two ferritic ductile cast irons (SiMo51, SiMo1000), one austenitic cast iron (D5S) and one austenitic cast steel (HK30), were included. The materials were mainly tested using three methods: stress relaxations with thermal cycling (SRTC), sequential tensile testing (STT) and the constant-load creep test (CL). Data sets generated by STT and SRTC generally agreed very well, but there were discrepancies compared with the CL tests.

When subjected to constant-load creep testing at 700 °C, the ferritic ductile cast iron SiMo51 showed more or less direct transitions between primary and tertiary creep. Creep cavities could be found around the graphite nodules and at the grain boundaries. Highly deformed areas showed large elliptical pores around the graphite nodules, a damage which was also found in the neck of tensile tested specimens.

The austenitic cast steel HK30 and the austenitic ductile cast iron D5S were constant-load creep tested at 750 °C. Both materials showed direct transition between primary and tertiary creep at higher stresses and more or less prolonged secondary creep at lower stresses. HK30 showed typical grain boundary creep-cavitation after long-term creep exposure. Sigma phase and G phase precipitated during creep. The cracks were intergranular and followed particle-matrix interfaces.

D5S showed large elliptical pores around graphite nodules when tested at higher stresses and delicate creep cavities around the nodules at lower stresses (similar to SiMo51). Various particles precipitated during creep exposure. Subgrain boundaries of 1° formed due to creep deformation. Final rupture occurred by shear cracks which propagated nodule-to-nodule.

8. Sustainability statement

The strive towards lower emissions in truck diesel- and gasoline engines has led to better engines in term of efficiency but also to higher temperatures of the exhaust gases. This development inevitably puts higher demands on the cast materials which are used for the application. Since creep deformation is one of the main degradation processes of the manifold materials, it is also essential to test the materials regarding their resistance against such exposure.

Referring to the 17 sustainable development goals set by the European Commission, this relates to: 7) affordable and clean energy, 9) industry, innovation and infrastructure, 11)

sustainable cities and communities, 12) responsible consumption and production and 13) climate action.

9. Acknowledgements

Regarding financing, the first part of the work (up to the licentiate degree) was completely financed by Scania CV AB. I am very grateful for this contribution.

The second part of the work (post-licentiate) was financed by a VINNOVA project, no. 2018-04019, “Inverkan av korrosion och krypning på utmattnings av värmebeständiga material till avgaskomponenter” within the research program “Fordonstrategisk Forskning och Innovation, FFI”, at VINNOVA, Swedish Governmental Agency for Innovation Systems. I am also very grateful for this governmental support and for the time the supervisors spent on writing the application.

Stefan Jonsson (main supervisor), is acknowledged for his contributions to appendices 1-5, for being a big inspiration as a researcher and supervisor, for teaching me a lot of new skills, for always being very careful and thorough in his review of my work, and for highly stimulating discussions.

Baohua Zhu (co-supervisor), is acknowledged for her contributions to appendices 1-5, for being highly supportive as a project leader, for teaching me about various sample preparation techniques, and for writing funding applications.

Joakim Lindblom, is acknowledged for teaching me a lot about materials science and testing methodology in general, for suggesting me to start spot welding the thermocouples, and for his theories regarding the speckle pattern tracking (4.2.2). Also, for taking me out sailing with the Wayfarer.

Henrik Östling, Taina Vuoristo and Mats Larsson are acknowledged for carrying out the creep tests. Henrik is especially acknowledged for providing a lot of insightful questions as opponent during my licentiate defense, for teaching me a lot about creep, and for being very helpful.

Joachim Hagström, is acknowledged for teaching me about EBSD, very beautiful imaging and for a very good collaboration.

Jan Linder, is generally acknowledged for fruitful discussions and for providing valuable suggestions.

Ralf Rablbauer, is acknowledged for arranging the STT tests, for arranging our visits to Volkswagen and for his contribution to appendix 2.

Marc Imiela is acknowledged for carrying out the STT tests at Volkswagen and for teaching me how to do the tests for a second round of tests.

Madeleine Ekström is acknowledged for fruitful discussions, for valuable previous contributions to the research field, and for introducing me to the topic.

Anders Tjernberg is acknowledged for a good collaboration (even though we could not publish) and for teaching me about a lot about creep and stress relaxations.

Peter Skoglund is acknowledged for lending me his test rig and for teaching me about testing methodology and TMF.

Jessica Elfsberg is acknowledged for helping with questions related to casting and nodule measurements.

Nulifer Ipek is acknowledged for being inspirational and highly supportive.

Lasse Miettunen is acknowledged for arranging his course in test programming and for being highly forthcoming in adjustments of the test rig used for SRTC.

Shengmei Xiang is acknowledged for co-operation in lab development.

Peter Szakalos is acknowledged for his valuable comments regarding the oxidation of SiMo51.

Rolf Sandström is acknowledged for teaching me about creep.

The group at Scania (YTMB) is acknowledged for being supportive, friendly and helpful.

The Workshop of Scania is acknowledged for doing parts of the sample preparation, and for being very helpful in this matter.

My colleagues at KTH, including other PhD students, are acknowledged for good comradeship.

My mother Heléne, my father Mikael and my brother Eric are acknowledged for unlimited support and help with everything outside of the PhD life.

Temporary colleagues at Adaptus Rehab AB, including Petra, Kristin, Fanny, Andrea and Andreas, are acknowledged for being a good company during my last time as a PhD student.

Close friends, including Petter, Carl and Wictor, are acknowledged for good times and good support.

10. References

- [1] V. Norman, Fatigue of Heavy-Vehicle Engine Materials, Doctoral thesis, Linköping: Linköping University, 2018.
- [2] F. Bruch, Thermo-mechanical fatigue of ductile iron, Masters thesis, Kassel: Institut für Werkstofftechnik, Metallische Werkstoffe, 2015.
- [3] N. Collin, Thermo-mechanical fatigue of cast iron for engine application, Masters thesis, Stockholm: KTH (Royal Institute of Technology), 2014.
- [4] H.-J. Kuhn, R. B and B. Skrotzki, "Thermomechanical fatigue of heat-resistant austenitic cast iron EN-GJSA-XNiSiCr35-5-2 (Ni-Resist D-5S)," *International Journal of Fatigue*, vol. 99, pp. 295-302, 2017.
- [5] M. Ekström, Oxidation and corrosion fatigue aspects of cast exhaust manifolds, Doctoral thesis, Stockholm: KTH (Royal Institute of Technology), 2015.

- [6] S. Xiang, S. Jonsson, B. Zhu and J. Odqvist, "Corrosion fatigue of austenitic cast iron Ni-resist D5S and austenitic cast steel HK30 in argon and synthetic diesel exhaust at 800°C," *International Journal of Fatigue*, vol. 132, pp. 1-11, 2020.
- [7] S. Xiang, High-Temperature Corrosion-Fatigue of Cast Alloys for Exhaust Manifolds, Licentiate thesis, Stockholm: KTH (Royal Institute of Technology), 2018.
- [8] S. Xiang, B. Zhu and S. Jonsson, "High-Temperature Corrosion-Fatigue Behavior of Ductile Cast Irons for Exhaust Manifolds Applications," *Materials Science Forum*, vol. 925, pp. 369-376, 2018.
- [9] S. Xiang, P. Hedström, B. Zhu, S. Jonsson and J. Odqvist, "Influence of graphite morphology on the corrosion-fatigue properties of the ferritic Si-Mo-Al cast iron SiMo1000," *International Journal of Fatigue*, vol. 140, 2020.
- [10] S. Xiang, S. Jonsson, P. Hedström, B. Zhu and J. Odqvist, "Influence of ferritic nitrocarburizing on the high-temperature corrosion-fatigue properties of the Si-Mo-Al cast iron SiMo1000," *International Journal of Fatigue*, vol. 143, 2021.
- [11] E. Hug, C. Keller, J. Favergon and K. Dawi, "Application of the Monkman-Grant law to the creep fracture of nodular cast irons with various matrix composites and structures," *Materials Science and Engineering A*, vol. 518, pp. 65-75, 2009.
- [12] A. Cottrell, An Introduction to Metallurgy, London: The Institute of Materials, 1975.
- [13] M. Ekström, P. Szakalos and S. Jonsson, "Influence of Cr and Ni on High-Temperature Corrosion Behavior of Ferritic Ductile Cast Iron in Air and Exhaust Gases," *Oxidation of Metals*, vol. 80, pp. 455-466, 2013.
- [14] A. Ebel, S. Yapi Brou, B. Malard, J. Lacaze, D. Monceau and L. Vaissiere, "High-Temperature Oxidation of a High Silicon SiMo Spheroidal Cast Iron in Air with In Situ Change in H₂O-content," *Materials Science Forum*, vol. 925, pp. 353-360, 2017.
- [15] Georg Fischer, "SiMo1000 Materials Data Sheet," Georg Fischer, 2014.
- [16] B. Piekarski and J. Kubicki, "Creep-resistant austenitic cast steel," *Archives of Foundry Engineering*, vol. 8, pp. 115-120, 2008.
- [17] M. Whittaker, B. Wilshire and J. Brear, "Creep fracture of the centrifugally-cast superaustenitic steels, HK40 and HP40," *Materials Science and Engineering A*, vol. 580, pp. 391-396, 2013.
- [18] S. Konosu, T. Koshimizu, T. Lijima and K. Maeda, "Evaluation of Creep-Fatigue Damage Interaction in HK40 Alloy," *Journal of Mechanical Design*, vol. 115, pp. 41-46, 1993.
- [19] M. Kassner, Fundamentals of Creep in Metals and Alloys, Butterworth Heinemann, 2015.

- [20] S. Manson and G. Halford, *Fatigue and Durability of Metals at High Temperatures*, ASM International, 2009.
- [21] S. Jonsson, *Mechanical Properties of Metals and Dislocation Theory from an Engineer's Perspective*, Stockholm: KTH (Royal Institute of Technology), 2010.
- [22] H. Östling, Interviewee, *Swerim, Private communication*. [Interview]. October 2020.
- [23] M. Ashby, C. Gandhi and D. Taplin, "Fracture-mechanism maps and their construction for F.C.C metals and alloys," *Acta Metallurgica*, vol. 27, pp. 699-729, 1979.
- [24] T. Tozera, O. Sherby and J. Dorn, *Trans. ASM*, vol. 49, p. 173, 1957.
- [25] F. Norton, *The Creep of Steels at high Temperatures*, New York: McGraw-Hill, 1929.
- [26] R. Sandström, "Creep Strength of austenitic stainless steels for boiler applications," *Coal Power Plant Materials and Life Assessment*, pp. 127-145, 2014.
- [27] H. Frost and M. Ashby, "Deformation-mechanism maps for pure iron, two austenitic stainless steels, and a low-alloy ferritic steel," *Fundamental Aspects of Structural Alloy Design*, 1977.
- [28] J.-O. Nilsson, P. Howell and G.L. Dunlop, "Interfacial microstructure and low stress, high temperature creep of an austenitic stainless steel.," *Acta Metallurgica*, vol. 27, pp. 179-186, 1979.
- [29] R. Swindeman, "The interrelation of Cyclic and Monotonic creep Rupture," in *International conference on creep*, London, Paper 32, pp. 71-76, 1963.
- [30] Å. Martinsson, H. Andersson-Östling, F. Settleam, R. Wui and R. Sandström, "Creep testing of nodular iron at ambient and elevated temperatures (nbr: R-10-64)," Swerea Kimab AB, Kista, 2010.
- [31] I. Hervas, A. Thuault and E. Hug, "Damage Analysis of a Ferritic SiMo Ductile Cast Iron Submitted to Tension and Compression Loadings in Temperature," *Metals*, vol. 5, pp. 2351-2369, 2015.
- [32] T. Sjögren, P. Vomacka and I. Svensson, "Comparison of mechanical properties in flake graphite and compacted graphite cast irons for piston rings," *International Journal of Cast Metals Research*, vol. 17, pp. 65-71, 2004.
- [33] M. Dong, C. Prioul and D. Francois, "Damage Effect on the Fracture Toughness of Nodular Cast Iron: Part 1. Damage Characterization and Plastic Flow Stress Modeling," *Metallurgical and Materials Transactions A*, vol. 28, pp. 1997-2245, 1996.
- [34] L. L. Liu, Q. Guo and Y. Niu, "Transition Between Different Oxidation Modes of Binary Fe-Si Alloys at 600-800C in Pure O₂," *Oxidation of Metals*, vol. 79, pp. 201-224, 2013.

- [35] M. Appelt, Eisen-Aluminium-Legierung für thermomechanisch belastete Komponenten im Abgasstrang (Doctoral thesis), Karlsruher institut für technologie, 2013.
- [36] P. Hähner, E. Affeldt, T. Beck, H. Klingelhöffer, M. Loveday and M. Rinaldi, "Validated Code-of-Practice for Strain-Controlled Thermo-Mechanical Fatigue Testing," European commission, Directorate General, Joint Research Centre, 2006.
- [37] A. Verma, M. Sundararaman, J. Singh and S. Nalawade, "A new method for determining the Curie temperature using a dilatometer," *Measurement Science and Technology*, vol. 10, pp. 105-106, 2010.
- [38] Swedish Institute of Standards, "Metallic materials - Uniaxial creep testing in tension - Method of test (ISO 204:2018)," Swedish Institute of Standards, 2018.
- [39] T. Seifert, R. Hazime and S. Dropps, "TMF Life Prediction of High Temperature Components Made of Cast Iron HiSiMo: Part II: Multiaxial Implementation and Component Assessment," *SAE International Journal of Materials and Manufacturing*, vol. 7, pp. 421-431, 2014.
- [40] T. Seifert, R. Hazime and S. Dropps, "TMF life prediction of high temperature components made of cast iron HiSiMo: Part I: uniaxial tests and fatigue life model.," *SAE International Journal of Materials and Manufacturing*, vol. 7, pp. 439-445, 2014.

